Recent Global Decline in Endorheic Basin Water Storage

Jida Wang[1 *], Chunqiao Song[2,3 *], John T. Reager[4], Fangfang Yao[1], James S. Famiglietti[4,5], Yongwei Sheng[3], Glen M. MacDonald[3,6], Fanny Brun[7,8], Hannes Müller Schmied[9,10], Richard A. Marston[1], Yoshihide Wada[11]

[1]Department of Geography, Kansas State University, Manhattan, KS 66506, USA.

[2]Key Laboratory of Watershed Geographic Sciences, Nanjing Institute of Geography and Limnology, Chinese Academy of Sciences, Nanjing, 210008, China.

[3]Department of Geography, University of California, Los Angeles, CA 90095, USA.

[4]Jet Propulsion Laboratory, California Institute of Technology, CA 91109, USA.

[5]Global Institute for Water Security, University of Saskatchewan, Saskatoon, SK S7N 3H5, Canada.

[6]Department of Ecology and Evolutionary Biology, University of California, Los Angeles, CA 90025, USA.

[7]University of Grenoble Alpes, CNRS, IRD, Grenoble INP, IGE, F-38000, Grenoble, France

[8]LEGOS, Université de Toulouse, CNES, CNRS, IRD, UPS, F-31400, Toulouse, France

[9]Institute of Physical Geography, Goethe University Frankfurt, 60438 Frankfurt am Main, Germany

[10]Senckenberg Biodiversity and Climate Research Center (SBiK-F), 60325 Frankfurt am Main, Germany

[11]International Institute for Applied Systems Analysis, A-2361 Laxenburg, Austria.

*JW and CS contributed equally to this work.

Contents

Supplementary Text

Validation of modeled snow water equivalent

Modeled monthly time series of snow water equivalent (SWE) is validated against the Snow Data Assimilation System (SNODAS)[1] data product (version 1, accessed from https://nsidc.org/data/g02158). SNODAS is a modeling and data assimilation system developed by the National Operational Hydrologic Remote Sensing Center (NOHRSC) of the NOAA National Weather Service. It provides some of the highest-quality estimates of snowpack properties, e.g., snow depth, SWE, temperature, and melt runoff, across the conterminous United States and southern Canada. Its spatial coverage includes ~60% of the total area of the endorheic North America (Fig. S19).

We processed the SNODAS SWE daily product (at 1 km spatial resolution) to monthly time series of average SWE (in mm) within the covered endorheic North America. The processed SNODAS SWE time series is compared with the region-average monthly SWE simulated by the seven hydrological models as described in Methods (also see Table S1). Considering that the SNODAS product is not available until late 2003, our validation is performed on the complete annual cycles (12 years) from April, 2004 to the end of our study period (March, 2016). Consistent with our methods for TWS partitioning, the modeled SWE trend is fitted from the output ensemble of CLM, Mosaic, Noah, VIC, and WGHM models, and the 95% confidence interval (CI) is propagated from (i) SWE variations among these five models, (ii) the discrepancy between the ensembles of the five models and all seven hydrological models (including CLSM and PCR-GLOBWB) til the end of 2014, and (iii) the residuals of linear trend fitting. The CI for the SNODAS trend is inferred from the residuals of its trend fitting alone.

As shown in Fig. S21a, modeled full SWE time series generally follow that of the SNODAS product, although the models tend to underestimate the seasonal maxima by an

average factor of ~2. The agreement between models and SNODAS appears to be overall improved after the removal of climatology (Fig. 21b). Significant Pearson correlations are found between deseasonalized SWE anomalies in SNODAS and each of the seven models: 0.62 with Mosaic, 0.63 with CLSM and Noah, 0.68 with CLM, 0.70 with VIC, 0.85 with PCR-GLOBWB, and 0.89 with WGHM (all *p*-values less than 0.01). The interannual trend in model-ensemble anomalies (–0.23 (±0.20) mm yr^{-1}) is fairly comparable to that of SNODAS (–0.09 (±0.30) mm yr^{-1}), with a discrepancy insignificant to the scale of their CIs. Whether this is true in other regions with larger snowpack, e.g. endorheic High Mountain Asia (HMA), remains uncertain. However, SWE changes in endorheic HMA have been included as part of glacier mass changes derived from stereo imagery (refer back to the main text), and the distribution of snowpack in arid/semiarid endorheic basins is overall rare. So we consider that the errors in modeled SWE have no considerable impacts on the partitioning of net endorheic TWS trends.

Validation of modeled soil moisture

We validate modeled monthly soil moisture (SM) time series against in situ SM measurements through the Soil Climate Analysis Network (SCAN) (accessed at www.wcc.nrcs.usda.gov/scan) administrated by the National Water and Climate Center of the USDA Natural Resources Conservation Service. Typically, a SCAN station monitors volumetric moisture content at various soil depths, together with some other energy and meteorological parameters (e.g., air temperature, relative humidity, and liquid precipitation). The standard soil depths include 2, 4, 8, 20, and 40 inches or about 5, 10, 20, 50, and 100 cm (a total of 5 layers).

There are currently ~200 SCAN stations across the US, including 43 stations within endorheic basins (Fig. S19). The available measurement period varies among the stations. To effectively validate our modeled SM trends, we use all 22 stations (red dots in Fig. S19) where each of the station records exceeds 5 consecutive years during our study period (2002–2016). All of these stations happen to be located in the Great Basin. IDs of the 22 SCAN stations are

labeled (in red) in Fig. S19, and their names and geographic coordinates are provided in Table S6.

As described in Methods, our SM trends are calculated from the ensemble of the four GLDAS LSMs (CLM, Mosaic, Noah, and VIC). For each LSM, SM values are integrated from the simulated water contents throughout the entire soil compartments (typically covering surface, vadose, and other subsurface layers). The soil compartment properties, however, are model-specific (see Table S1). The maximum soil depth ranges from 1.9 m in VIC to 3.4 m in CLM, which all exceed the maximal depth measured by the SCAN stations (~1 m). The total soil layer number ranges from 3 in VIC and Mosaic to 10 in CLM, and the depths of individual layers are not always consistent with those of the SCAN measurements. These factors cause some challenges in the SM validation. As a solution, we compare the modeled and in situ volumetric SM contents (in %) instead of absolute water depths. For each station, we calculate (i) the correlation between deseasonalized in situ and model-ensemble monthly SM anomalies integrated through their total soil layers, and (ii) both the correlation and interannual trends in the SM anomalies for the soil layer of 0–10 cm. We focus on the top 10 cm soil because this layer is the most commonly available: it is shared by the SCAN stations and three of the four LSMs (CLM, Noah, and VIC).

As shown in Table S6, out of the 19 SCAN stations where measurements are available for at least 5 consecutive years in all soil layers, 17 stations have in situ measurements that are significantly correlated ($p < 0.05$) with our model-ensemble anomalies. Out of the 22 stations where measurements of over 5 consecutive years are available for the top 10 cm soil, 21 stations have in situ measurements significantly correlated with the modeled anomalies, and the correlations remain significant for 20 of them when the significance level (α) is lowered to 0.01.

Although the SCAN measurements provide an important in situ validation source, their measurements are made at each station site while our modeled SM contents represent the condition of the model pixel (0.25 degree or coarser) that includes the station site. Such spatial

inconsistency causes inevitable discrepancies between modeled and in situ SM contents. Even though, the interannual trends in modeled and in situ time series for the top 10 cm soil are comparable for most of the 22 SCAN stations (Table S6 and Fig. S20). The SM change rates (the fitting slopes) show insignificant difference to their CIs for 13 stations. If we also include the impact of fitting intercept, the modeled and in situ trends overlap each other in the tolerance of their CIs for 17 out of the 22 stations.

It is worth noting that GLDAS LSMs do not include human processes, so our calculated SM trends do not account for the impacts of groundwater-fed or surface-water-fed irrigations. Irrigated areas cover ~10% or much less of the arid/semiarid regions (according to the Global Map of Irrigation Areas (GMIA, www.fao.org/nr/water/aquastat/irrigationmap/index60.stm)[2,3]. The purpose of irrigation is to supplement local SM and satisfy the crop's biophysical demands (e.g., for transpiration) during the growing season. Excess irrigation (water exceeding the crop's immediate consumption) can temporarily increase the local SM. If the soil is saturated, the excess water will be drained, evaporated, or percolate to the groundwater table. The remnant moisture supplement may eventually be consumed by the crop, rather than changing long-term SM. For these reasons, we assume that during the GRACE period, direct irrigation impacts on SM were regional and transient (e.g., limited to monthly to seasonal timescales), and did not substantially alter the inter-annual SM trends at the studied zonal to global scales. We here acknowledge that the accumulated impact of irrigation could be more substantial over the past century or several decades, due to rapid expansion of irrigated areas since ~1950s[4]. Existing studies also showed that altered water and energy budgets by irrigation could increase precipitation via surface-atmosphere coupling, which in turn affected SM[5-7]. However, such impacts on precipitation and energy budgets may have been integrated to the GLDAS climate forcing inputs.

Linkage of water storage changes to climate variability

Periodic variability of the climate system can strongly influence regional meteorological patterns and the associated TWS[8-10]. Recent studies showed that detrended interannual TWS variations during the GRACE era were correlated with the El Niño-Southern Oscillation (ENSO) over much of the globe, particularly tropical and subtropical regions (e.g., the Amazon and Southeast Asia). In these analyses, the calculated trend was usually removed from the deseasonalized TWS time series to isolate interannual signals, assuming that the trend was mainly induced by "secular" climate change and/or direct human impacts rather than interannual climate variability[11-13]. Although this is valid for many cases, cautions are needed when associating detrended TWS with climate variability during a relatively short period. For example, the first decade after 2000 (till 2012 or so) favored La Niña episodes more than El Niño, leading to excess precipitation on land and a hiatus in sea level rise[14]. This ENSO asymmetry, an effect of interannual climate variability, contributed to a net decadal increasing trend in the TWS (excluding ice sheets and glaciers) on the global continental surface[15,16].

Given this caveat, we compare the intensity of climate variability with deseasonalized TWS anomalies (hereafter TWSA) without removal of the linear trend. As such, a strong correlation between TWSA and climate variability suggests the importance of climate variability on TWS variations despite the possible existence of secular factors (e.g., global warming and groundwater depletion). Similarly, a weak correlation, in combination with a strong TWS trend, implies a possible dominance of the effect of more secular factors over that of short-term climate variability. Importantly, we here do not aim at a quantitative separation of the effect of climate variability from that of secular factors, but to examine whether climate variability may considerably contaminate or determine our observed endorheic TWS decline.

We here examine five prominent modes of climate variability related to sea surface temperature or pressure anomalies in the Pacific, Atlantic, or Indian Oceans (Fig. S12; Table S4). They include ENSO, North Atlantic Oscillation (NAO), Pacific Decadal Oscillation (PDO),

Indian Ocean Dipole (IOD), and Atlantic Multidecadal Oscillation (AMO). Among them, ENSO and NAO exhibited clear interannual variability in the GRACE era, where warm/cool (positive/negative) phases shifted at annual to quadrennial frequencies. The periodicity of PDO ranges from multiyear to decadal timescales[17]. During the GRACE era, a duration of ~3–5 years is observed in either phase. These timescales are shorter than our studied 15 years (2002–2016), thus allowing for a valid investigation of the possible link between TWS and each of the three modes. IOD is usually considered as a mode of interannual variability[18]. However, it had experienced no major negative events since the mid-1990s until the latter half of 2016[19]. This positive IOD period was accompanied by a similarly enduring warm phase in AMO, which typically fluctuates at long-term (multidecadal) timescales[20]. We include IOD and AMO, both varying at low frequency in the GRACE era, to only consider their possible impacts on TWS changes at interannual or subdecadal timescales[21]. Monthly/bimonthly time series of each climate index is acquired from the archive of the NOAA's Earth System Research Laboratory (www.esrl.noaa.gov/psd/data/climateindices/list; Table S4).

For each climate index, we calculate its correlation with TWSA in both global exorheic/endorheic basins and the 10 regional endorheic zones. On a basin scale, the flux of TWS (i.e., ΔTWS between each time interval) reflects the residual between precipitation (the source), and evapotranspiration and runoff (the sinks). Numerous studies suggested that climate variability strongly influences precipitation anomalies in various regions[9,21-27]. As runoff and evapotranspiration depend on the availability of precipitation, their anomalies are also affected by climate variability[11]. However, the sink rates are not solely determined by contemporaneous weather conditions (e.g., precipitation inputs). They are often related to the status of historical land water storage (e.g., baseflow and lake/wetland water detention), which can result in evident time lags between climate index and TWS flux. When the climate index misrepresents the contribution of the sinks, we may observe the index to (lag-)correlate with TWSA more than ΔTWSA (changes between consecutive TWSA)[11,13], given that TWS

integrates ΔTWS and the previous TWS related to the sinks. For this reason, we explore the correlations between each climate index with both TWSA and ΔTWSA. To target interannual scales, time series of climate index and TWSA are smoothed by an average low-pass filter with a 13-month window. The Pearson correlation coefficients (*r*) are then computed between filtered climate index and TWSA/ΔTWSA time series for different time lags at a monthly step. We here constrain the lag within one year, following a range of ~3–12 months as applied/implied in some existing studies[11,13,21,28].

Figure S12 shows the time series of each climate index superimposed by global exorheic and endorheic TWSA. For the purpose of visual comparison, TWSA are phase-adjusted by the time lags that yield the maximum correlations with climate indices. On a global scale, exorheic TWSA is negatively correlated to ENSO modulations (measured as Multivariate ENSO Index (MEI)), whereas endorheic TWSA is, in a smaller magnitude, positively correlated (Fig. S12a). This contrast in correlation sign is consistent with the finding between tropical and arid regions by Phillips et al[11]. The strong correlation between MEI and exorheic TWSA (r = –0.73) is manifested by their signature resemblance, where positive/negative TWSA values synchronize with major La Niña/El Niño events (e.g., in 2007–2008, 2010–2012, and 2014–2016) with a lag of ~3 months. In comparison, endorheic TWSA is less sensitive to ENSO modulations, given a much weaker correlation (r = 0.27) and a longer lag duration.

The pattern of TWSA with PDO is similar to that with ENSO (Fig. S12c), except that the correlation between PDO and exorheic TWSA is more moderate (r = –0.54). This conforms to the fact that PDO is inherently related to ENSO at interannual timescales, but includes additional variability at decadal timescales[21]. A moderate correlation with exorheic TWSA is also found for NAO (r = –0.52, Fig. S12b). Similar to ENSO and PDO, the signature of NAO time series captures the positive exorheic anomaly in 2009–2010, but also shares similarities with small-amplitude interannual fluctuations such as in 2004–2006 and 2011–2012. However, its correlation with endorheic TWSA remains weak (r = –0.17).

As described previously, phases in IOD and AMO have been mainly positive during our study period, although recent studies identified a strong negative IOD in late 2016[19] and a likely emerging cold phase in AMO[29]. Apparently, the limited GRACE era precludes a diagnostic comparison between their full-cycle variations and TWS observations. Based on our results (Fig. S12d–e), no strong correlation is identified between global endorheic/exorheic TWSA and either of the two indices at interannual timescales after 2002 (magnitudes of *r* less than 0.60). Despite some short-term signature resemblance, such as between AMO and endorheic TWSA in 2003–2007 and between AMO and exorheic TWSA in 2010 and 2014, these similarities are overall transient and/or discontinuous during the process of the endorheic TWS decline.

In Table S4, we also report the maximum (lag-)correlations between each climate index and ΔTWSA in global exorheic/endorheic basins. The correlations are overall weaker than those with TWSA, but presents a consistent pattern that the global endorheic TWS is generally less correlated to interannual climate variability.

Although endorheic TWS is less sensitive to interannual variability on a global scale, it is important to note that stronger correlations exist in some regional endorheic zones (Table S4). For example, in Dry Andes and Patagonia, TWSA is strongly correlated with ENSO and PDO ($r \geq 0.60$) and moderately correlated with NAO ($r = 0.55$). TWSA in the Inner Tibet Plateau (ITP) is negatively correlated to PDO and ENSO, and to a lesser extent, positively correlated to IOD. In endorheic North America, TWSA shows moderate to strong correlations to all climate indices except IOD. Moderate linkages to multiple internanual indices (ENSO, NAO, and PDO) are also found in Australia and Great Rift Valley/Southern Africa (GRVSA). These results imply that climate variability, at least on interannual to subdecadal timescales, may exert important influences on the above-mentioned endorheic regions, which is generally consistent with existing literature[11,15,22,27,30-33]. However, these regions are limited in area (accounting for 31% of the global endorheic area), and include some of the endorheic zones where TWS declines are less dramatic (e.g., Australia and North America), or TWS experienced increasing trends (e.g.,

ITP and GRVSA). As a result, they end up with a net but uncertain TWS increase of 5.5 (±6.1) Gt yr^{-1} (Table 1). In comparison, the remaining regions in Sahara/Arabia and Central Eurasia (except ITP), the dominant contributors to the global endorheic TWS decline, are overall less correlated to interannual climate indices, which likely suggests substantial impacts from more secular factors such as human water managements. Again, this is largely consistent with recent literature[15,33,34], and also corroborated by our finding that 45% of the net TWS decline in Sahara/Arabia and Central Eurasia is attributed to groundwater depletion (Table 1).

In addition to correlations, we perform another experiment to test whether the times series of each climate index may produce a linear trend which is similar to that of endorheic TWSA. Given any endorheic zone, we simply scale the time series of each index to that of TWSA using a polynomial regression. We then calculate the linear trend and its 95% CI for each scaled index series, and compare them with the trend and CI for the GRACE-observed TWSA. Except endorheic Australia, we found that no scaled climate index, for any endorheic zone, produces a trend that is statistically similar to the observation (that is, the difference between scaled and observed trends insignificant to the CIs).

As major findings of this paper, we show that the recent decadal decline in endorheic TWS is substantial, and it stems from comparable losses in all three primary water storage components (surface water, soil moisture, and groundwater). This partitioning, together with zonal comparisons with climate variables (e.g., precipitation and temperature in Fig. S13), implies that the endorheic TWS decline is a complicated result of climate variability and forced responses (e.g., to anthropogenic climate change and direct human activities). Except the partitioning among water storage components, a definite decoupling between the contributions of climate variability and forced responses is beyond the scope of this study. Therefore, our reported TWS trend may not imply a continuous secular signal that can be extrapolated into the past or future. We also acknowledge that the current GRACE era prohibits a secure linkage of available TWS observations to any lower-frequency climate variability or secular trend.

Nevertheless, our exploration does indicate that compared to exorheic basins, TWS in the continental interiors (endorheic basins) is overall less sensitive to some prominent modes of climate variability at interannual timescales. This comparison highlights the important influences of human water management and longer-term climate conditions (e.g., (multi)decadal variability and anthropogenic warming), in addition to interannual variability of the natural climate system.

It is entirely possible that the recent decadal trend in global endorheic TWS may be altered by future climate variability. But the core message of our findings undeniably conveys that, even though the total water mass in the arid endorheic system may be limited, its change at least at the studied decadal timescale could be so substantial that it largely outpaced that in the entire exorheic landmass and signified a potential impact on the sea level budget. From this considerable decadal decline, we hereby suggest to the geoscience community the importance of a continued monitoring and understanding of TWS changes in the global endorheic system. A meaningful start is to look into how different water storage components contribute, as we demonstrate in this work.

Supplementary Figures

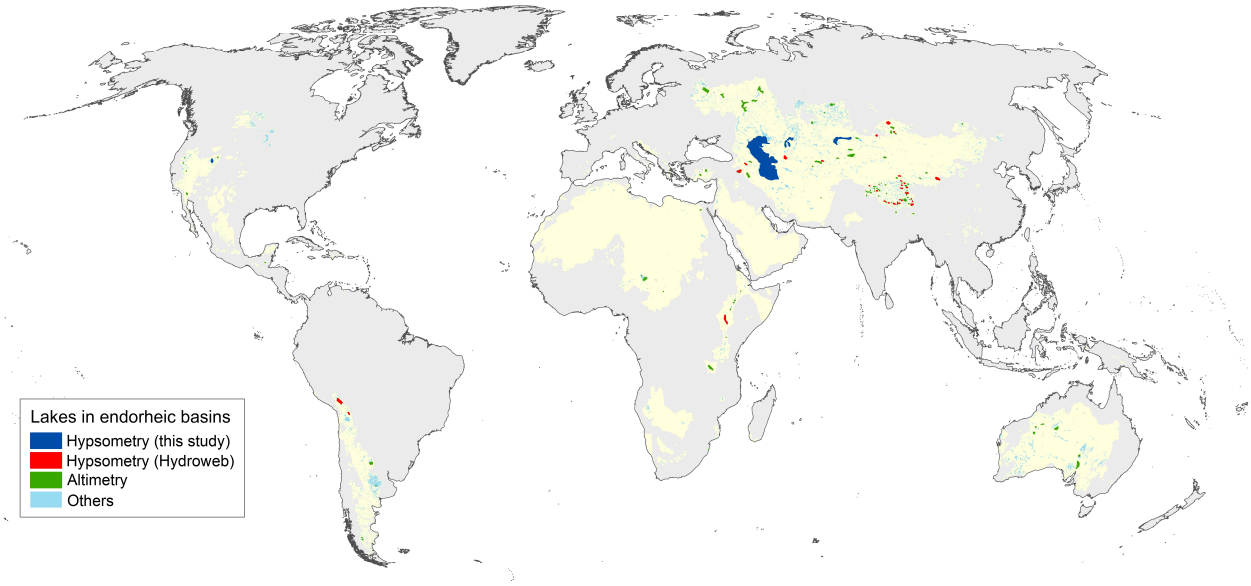

Figure S1. Lakes and reservoirs in global endorheic regions. Displayed water bodies are lakes and reservoirs larger than ~0.4 hectare across global endorheic basins, mapped and quality-assured using recent archival Landsat imagery[35]. Water storage changes are estimated for 142 major lakes (in blue, red, and green) where available altimetry level records during 2002–2016 are retrieved from the Hydroweb[36] (http://hydroweb.theia-land.fr), DAHITI[37] (http://dahiti.dgfi.tum.de/en), and G-REALM (https://ipad.fas.usda.gov/cropexplorer/global_reservoir) databases (level data accessed around November, 2016). Hypsometry is considered in storage estimation for 38 lakes, where level-area curves for 8 lakes (blue) are calibrated in this study (see Figs. S3–S10) and curves for the other 30 lakes (red) are retrieved from the Hydroweb. Storage changes in each of the other 104 lakes (green) are estimated by their level time series integrated with a static water extent mapped from Landsat images in 2008–2009 representing the intermediate storage condition during the study period. These lakes cover ~75% of the total surface water area in global endorheic basins. Storage changes in the other lakes (cyan) are considered as uncertainties. See Methods for more details.

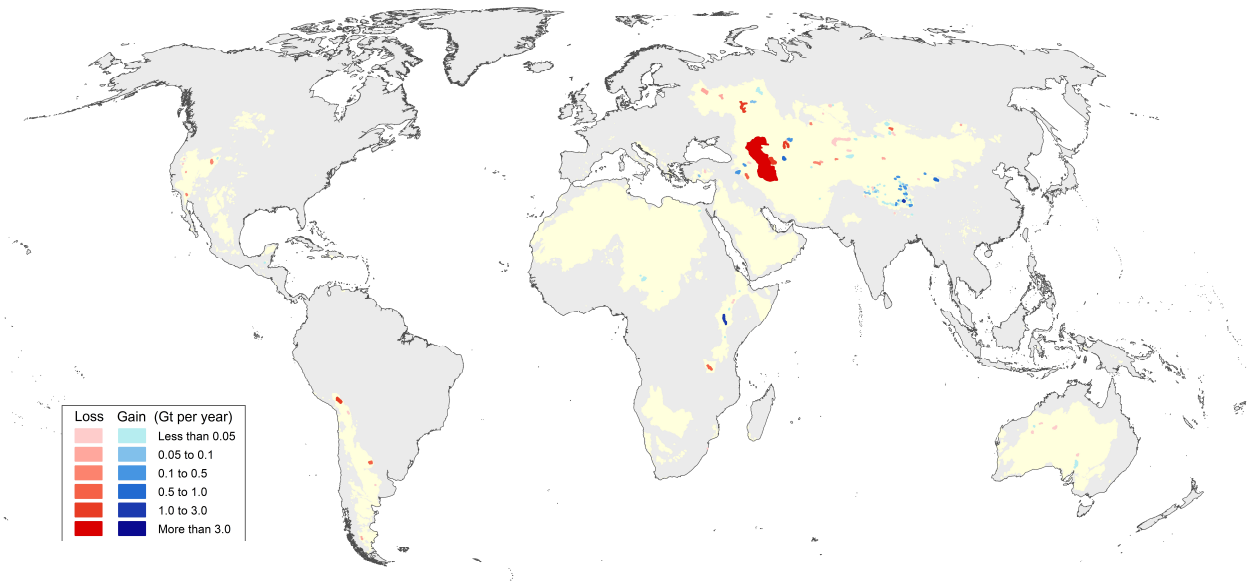

Figure S2. Water storage changes in major lake and reservoirs from April 2002 to March 2016. Shown are the 142 lakes with altimetry records (colored in red, blue, and green in Fig. 1S).

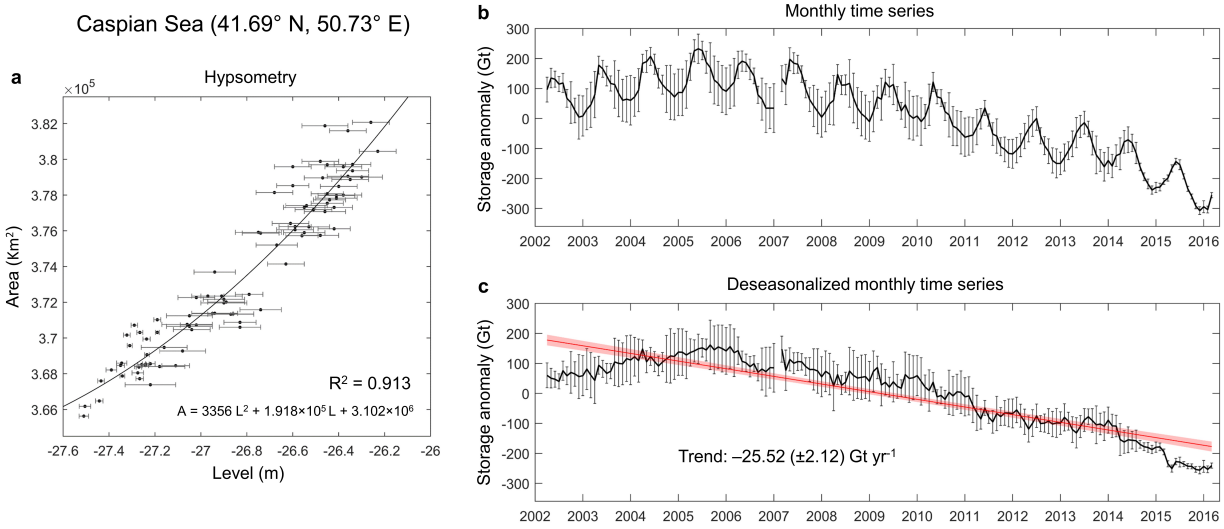

Figure S3. Water storage changes in Caspian Sea from April 2002 to March 2016. (**a**) Calibrated level-area hypsometric curve, where time series levels are acquired from multi-mission altimeter observations archived in the Hydroweb database and water inundation extents are mapped from the MODIS Terra 250-m surface reflectance 8-day composite imagery (MOD09Q1). Level values are meters above the surface reference (EGM2008 for Hydroweb[36]). Water levels are paired with mapped areas with a temporal tolerance of 8 days. Levels are averaged if more than one level measurements are available available within any 8-day window. Horizontal error bars represent the scales of level errors reported in the source altimetry data. The labeled hypsometric equation is fitted from the plotted level-area pairs, so it may not be suitable for extrapolating or representing hypsometry of the same lake beyond the plotted level-area ranges. For the same reason, we do not account for mapping-induced volume uncertainties arising from below the minimum water level during the study period (see Methods section “Estimating lake storage changes”). (**b**) Monthly time series of estimated lake storage anomaly (gigatons of water) (i.e., departures from the period mean). When no altimetry level is available for an 8-day window, water areas mapped from high-quality MODIS images (if available) are used to inverse water levels using the calibrated hypsometric curve. All measured/inversed water levels are used to derive the 8-day volume anomaly time series, which is further averaged to generate the monthly anomalies. (**c**) Monthly time series of deseasonalized lake storage anomaly. Vertical error bars and shades represent 95% confidence intervals (two standard deviation uncertainties) for water storage anomalies and best-fit linear trends, respectively. See “Methods” for more detailed uncertainty propagation.

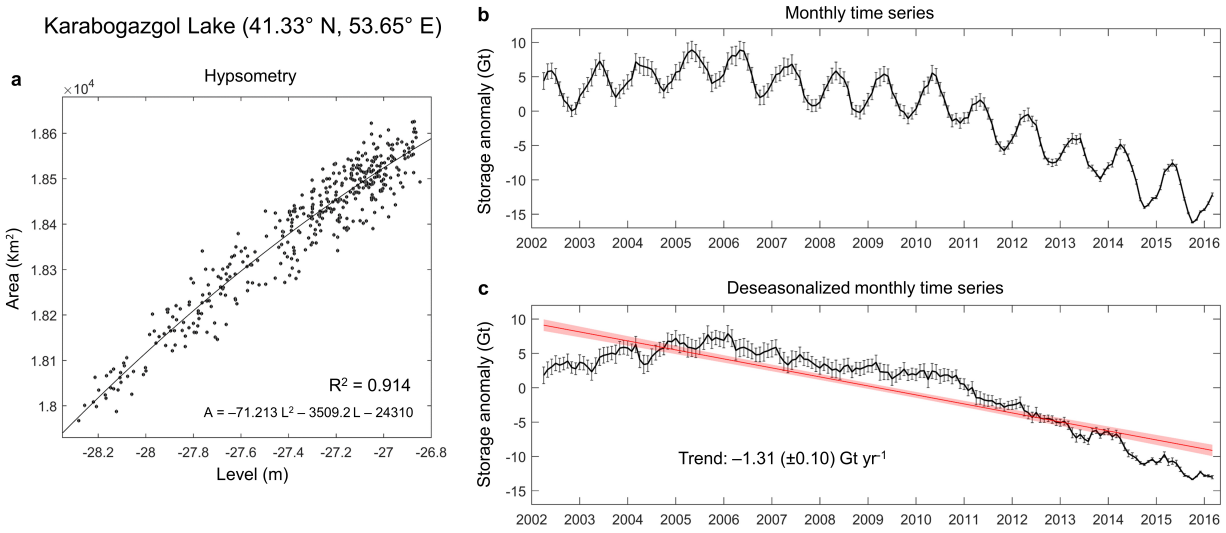

Figure S4. Water storage changes in Karabogazgol Lake from April 2002 to March 2016. (**a**)–(**c**) As in Fig. S3, except that lake water levels are acquired from DAHITI and the level values are expressed as meters above the geoid model EIGEN-6c3stat[37].

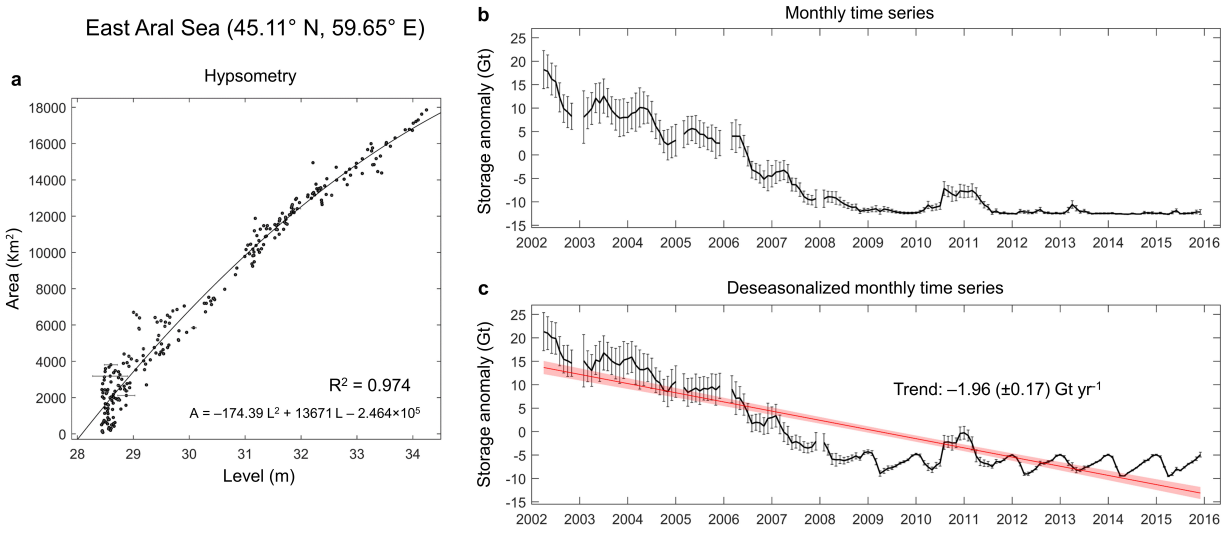

Figure S5. Water storage changes in East Aral Sea from April 2002 to March 2016. (**a**)–(**c**) As in Fig. S3, except that lake water levels are acquired from DAHITI and the level values are expressed as meters above the geoid model EIGEN-6c3stat.

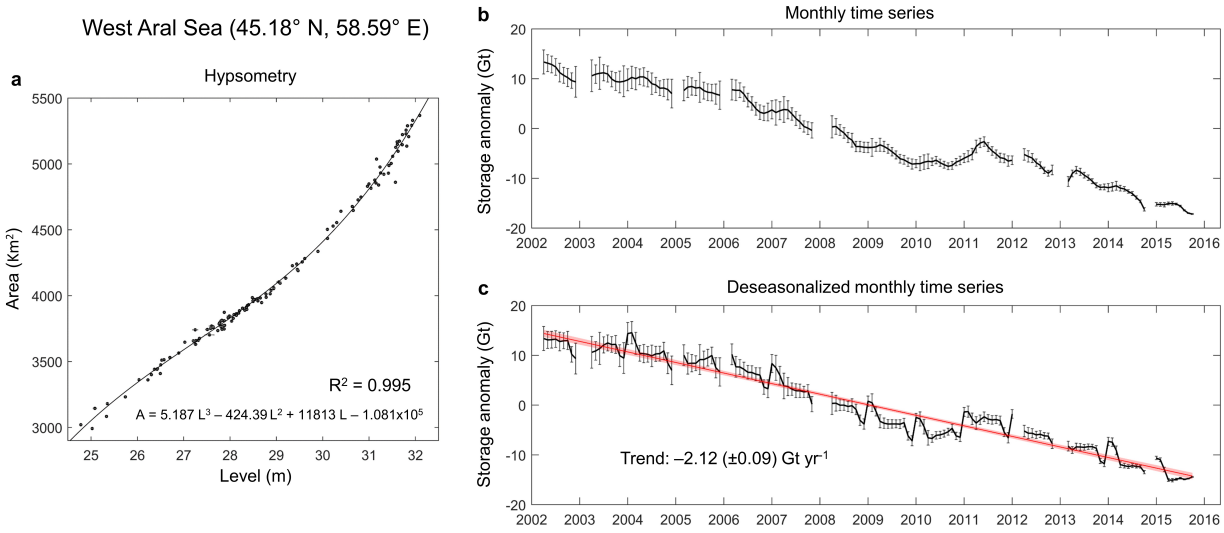

Figure S6. Water storage changes in West Aral Sea from April 2002 to March 2016. (**a**)–(**c**) As in Fig. S3, except that lake water levels are acquired from DAHITI and the level values are expressed as meters above the geoid model EIGEN-6c3stat.

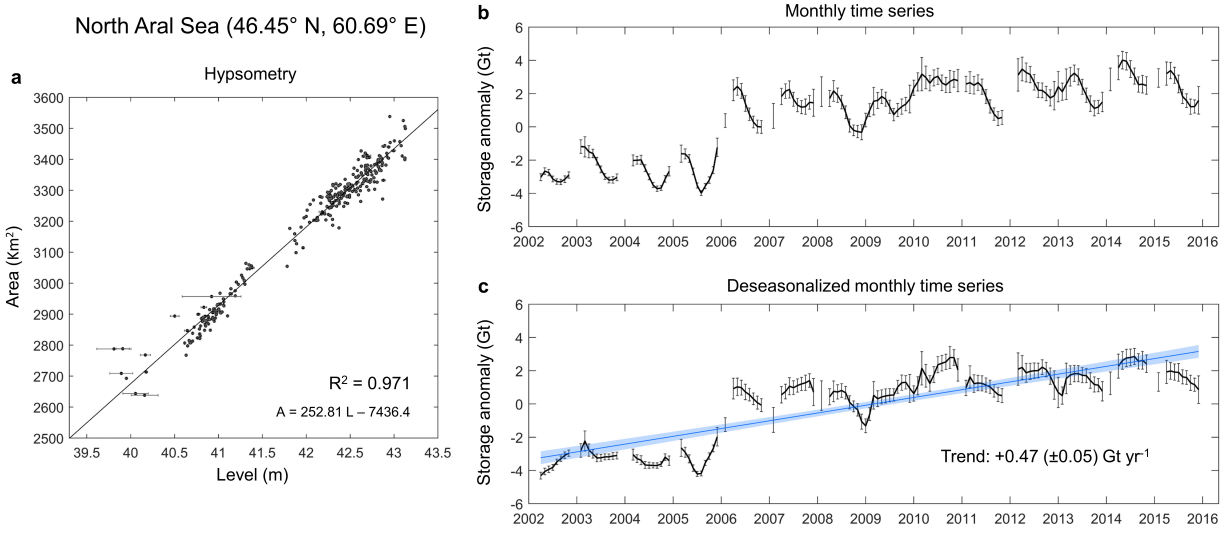

Figure S7. Water storage changes in North Aral Sea from April 2002 to March 2016. (**a**)–(**c**) As in Fig. S3, except that lake water levels are acquired from DAHITI and the level values are expressed as meters above the geoid model EIGEN-6c3stat.

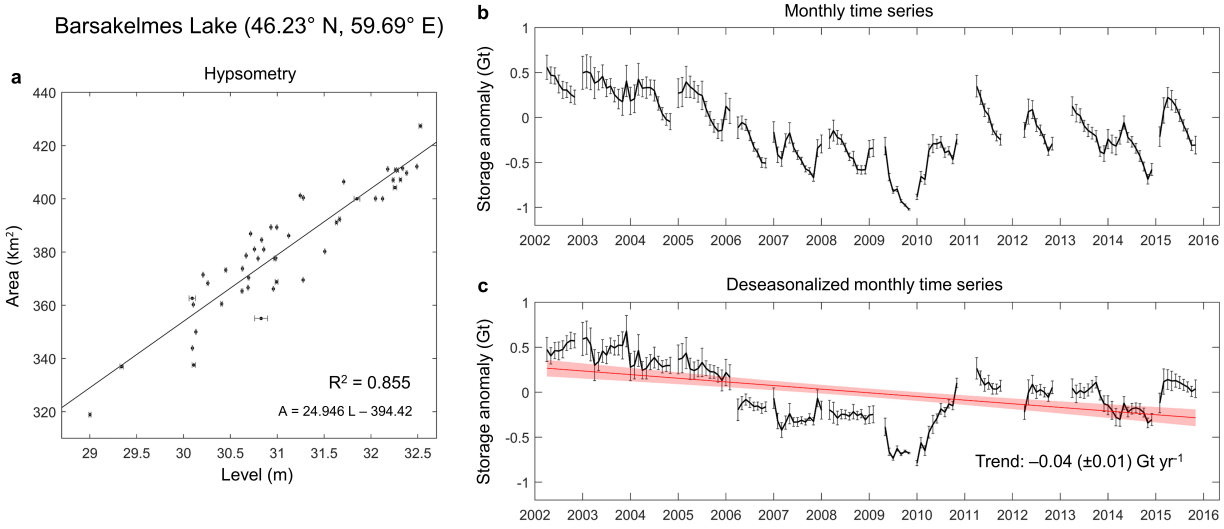

Figure S8. Water storage changes in Barsakelmes Lake from April 2002 to March 2016. (**a**)–(**c**) As in Fig. S3, except that lake water levels are acquired from DAHITI and the level values are expressed as meters above the geoid model EIGEN-6c3stat.

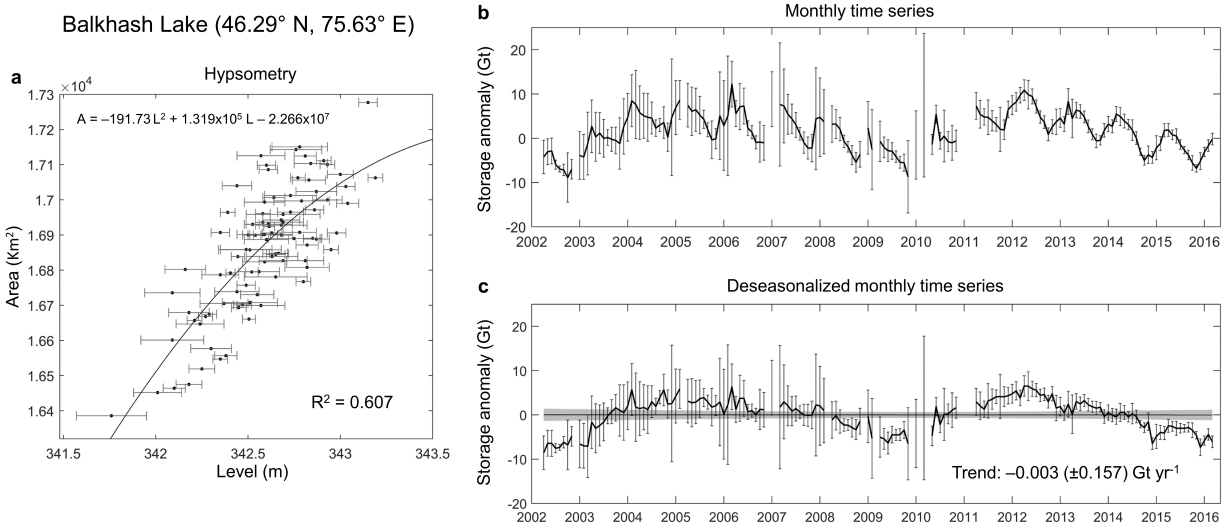

Figure S9. Water storage changes in Balkhash Lake from April 2002 to March 2016. (**a**)–(**c**) As in Fig. S3.

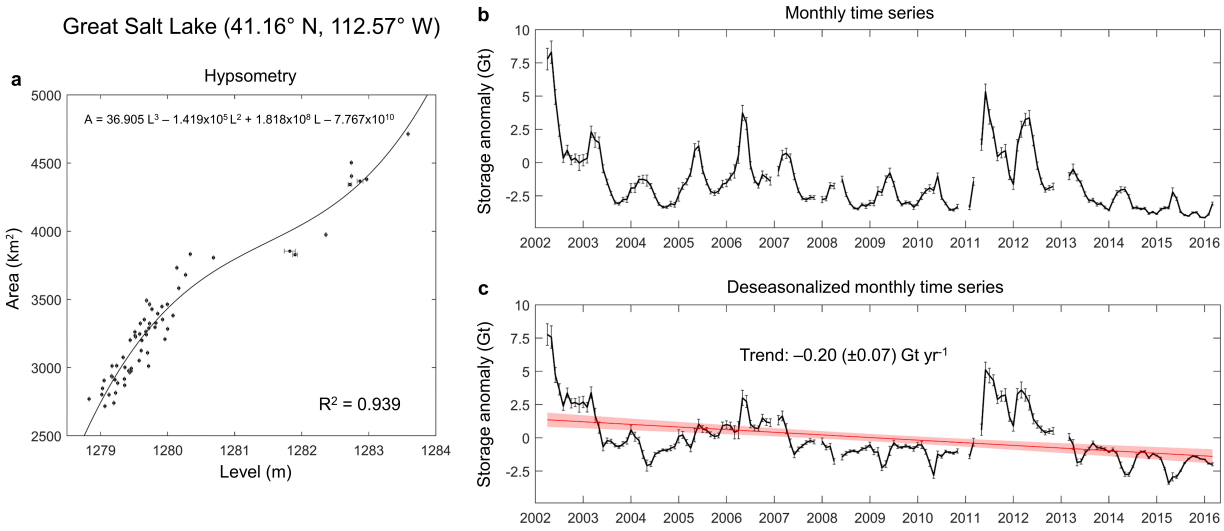

Figure S10. Water storage changes in Great Salt Lake from April 2002 to March 2016. (**a**)–(**c**) As in Fig. S3, except that lake water levels are acquired from DAHITI and the level values are expressed as meters above the geoid model EIGEN-6c3stat.

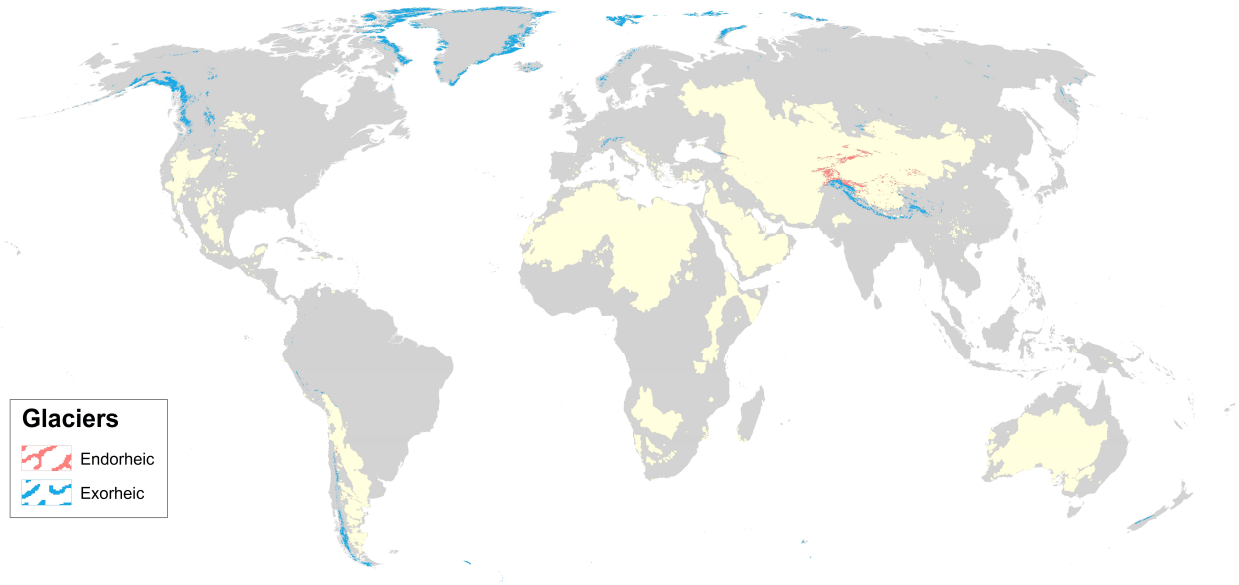

Figure S11. Global glacier extents according to the Randolph Glacier Inventory (RGI 6.0)[38]. Red and blue polygons represent the extents of glacierized regions within endorheic and exorheic basins, respectively. Yellow areas indicate endorheic basins. The global glacier extents cover a total area of ~750 thousand km^2. About 7% (~50 thousand km^2) is within endorheic basins, most of which (98%) is distributed across the High Mountain Asia.

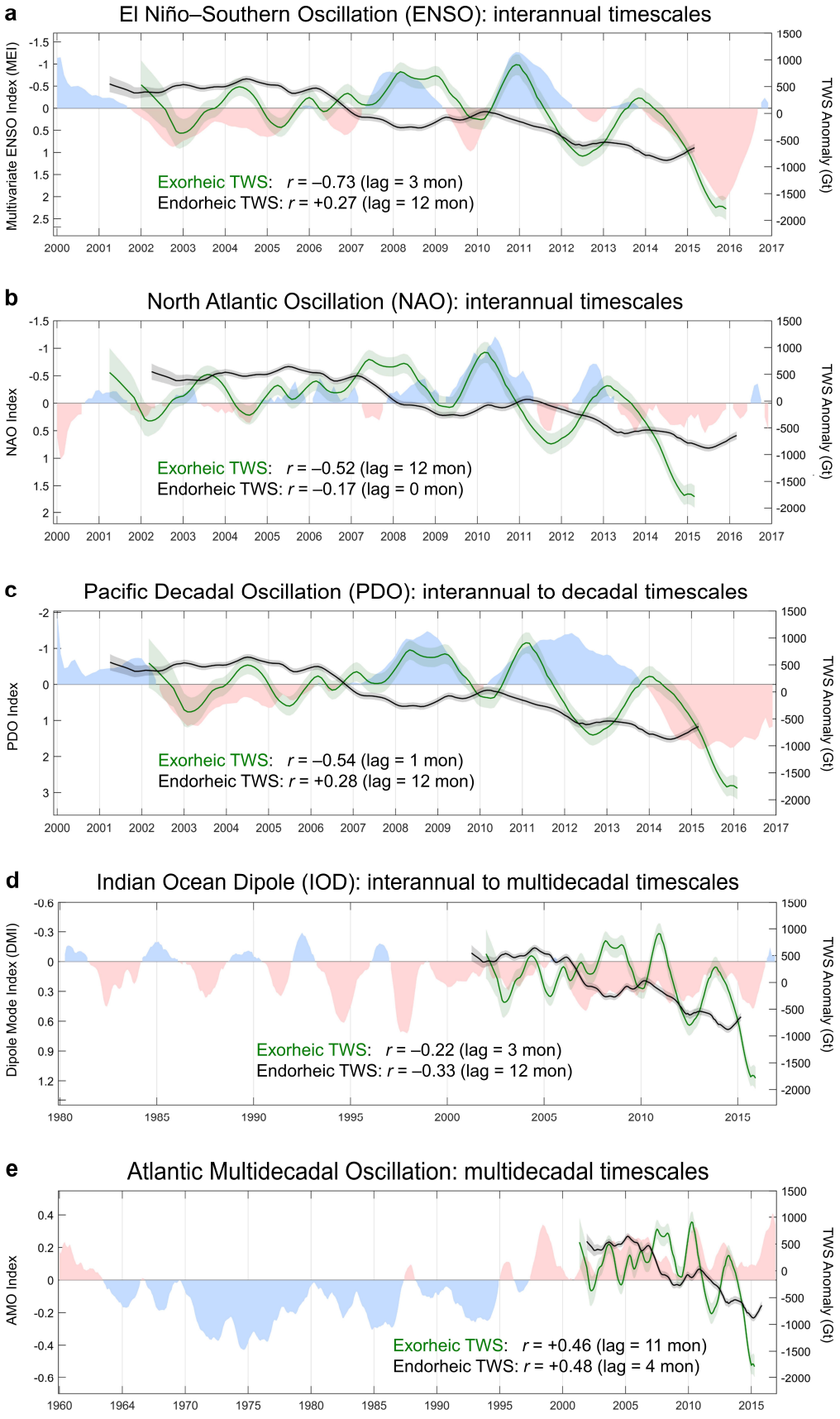
a
El Niño–Southern Oscillation (ENSO): interannual timescales
Multivariate ENSO Index (MEI)
TWS Anomaly (Gt)
Exorheic TWS: r = –0.73 (lag = 3 mon)
Endorheic TWS: r = +0.27 (lag = 12 mon)
b
North Atlantic Oscillation (NAO): interannual timescales
NAO Index
TWS Anomaly (Gt)
Exorheic TWS: r = –0.52 (lag = 12 mon)
Endorheic TWS: r = –0.17 (lag = 0 mon)
c
Pacific Decadal Oscillation (PDO): interannual to decadal timescales
PDO Index
TWS Anomaly (Gt)
Exorheic TWS: r = –0.54 (lag = 1 mon)
Endorheic TWS: r = +0.28 (lag = 12 mon)
d
Indian Ocean Dipole (IOD): interannual to multidecadal timescales
Dipole Mode Index (DMI)
TWS Anomaly (Gt)
Exorheic TWS: r = –0.22 (lag = 3 mon)
Endorheic TWS: r = –0.33 (lag = 12 mon)
e
Atlantic Multidecadal Oscillation: multidecadal timescales
AMO Index
TWS Anomaly (Gt)
Exorheic TWS: r = +0.46 (lag = 11 mon)
Endorheic TWS: r = +0.48 (lag = 4 mon)

Figure S12. Comparisons between climate variability and global exorheic/endorheic TWS anomalies. Right y-axis shows deseasonalized monthly TWS anomalies in global exorheic (green) and endorheic (black) basins (transparent shades illustrate 95% CIs), while left x-axis shows monthly time series of climate index for (**a**) El Niño-Southern Oscillation (ENSO), (**b**) North Atlantic Oscillation (NAO), (**c**) Pacific Decadal Oscillation (PDO), (**d**) Indian Ocean Dipole (IOD), and (**e**) Atlantic Multidecadal Oscillation (AMO). Red/blue shades illustrate warm/cool (positive/negative) phases. Refer to Table S4 for the source of each climate index. For each panel, time series of both climate index and TWS anomalies are smoothed by an average low-pass filter with a window size of 13 months. Each TWS time series is phase-shifted by the time lag (in months) that produces the maximum Pearson correlation (*r*) between the TWS anomalies and the climate index (text-labeled on each panel). In addition to our study period (April 2002 to March 2016), we further acquire monthly TWS anomalies (from JPL-RL05M version 2) for the following six months (April–September 2016), in order to effectively filter TWS anomalies in the last six months of our study period (October–December 2015 and January–March 2016). This extension is similarly done for the filtering of each climate index. Since no TWS observations were available before April 2002, time series in the first six months of our study period (April–September 2002) are filtered using available values (as shown in this figure) but are removed from correlation calculations.

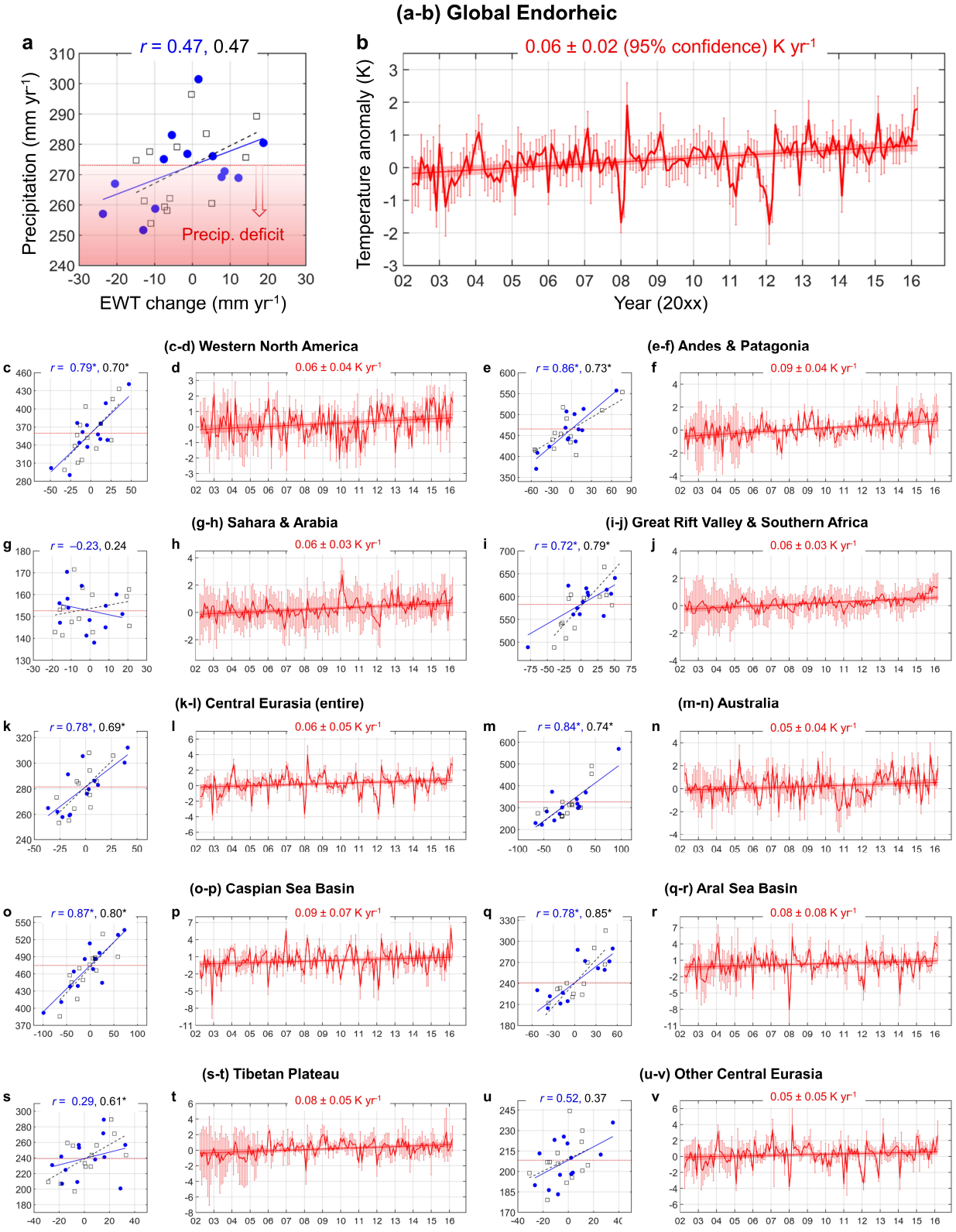

Figure S13. Endorheic TWS changes in response to climate variables. (**a**–**b**) Global endorheic system. (**c**–n) Primary continental zones. (**o**–**v**) Secondary zones in Central Eurasia.

For each enumeration region, the left panel illustrates the scatter plot between the net change in equivalent water thickness (EWT) and total precipitation for each year (blue dots). The relationship is evaluated on an annual basis in order to remove the correlation due to seasonal impacts. Considering that the initial GRACE observation was available in April 2002, we define a full annual cycle as starting from April and ending in March of the next year. *r* shows the Pearson correlation coefficient between annual net EWT changes (integrated variations within each annual cycle) and total precipitation, and asterisks indicate significant correlations with $\alpha = 0.05$. Positive correlations are observed in the global endorheic system and most continental zones except a weak negative correlation in Sahara and Arabia (g). To test the pattern consistency, we recalculate the relationship for each region by using net EWT changes and total precipitation in each full calendar year (January to December for 2003–2015; black squares). The general relationships remain similar, except that in Sahara and Arabia, the previous negative correlation becomes weakly positive, implying a likely minor impact of precipitation on its recent TWS changes (which is consistent with the dominant groundwater contribution seen in Fig. 4). For each region, the red horizontal line approximates the period-average precipitation level on which EWT change is 0. Theoretically, this precipitation level meets the demand for evapotranspiration, and maintains the overall water budget equilibrium in the endorheic region. Precipitation below or near the equilibrium line may lead to possible water budget deficits. Right panels illustrate monthly temperatures and 95% uncertainties from April 2002 to March 2016. Quantified temperature trends confirm that warming has prevailed in each of the endorheic zones, with an average rate of 0.06 K yr^{-1} exceeding the global average of approximately 0.02 K yr^{-1} [39].

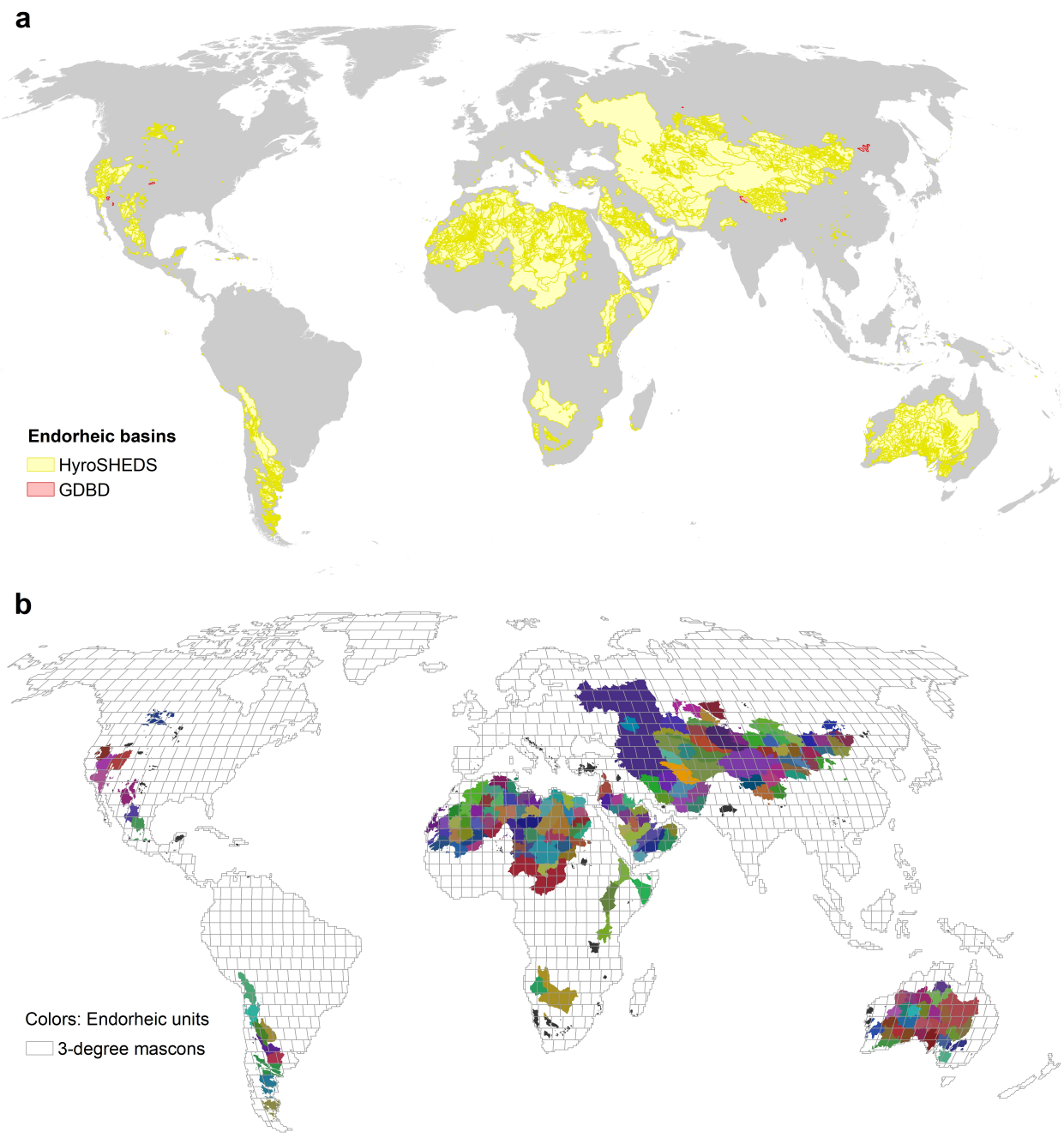

Figure S14. Global endorheic basins and units. (**a**) Detailed endorheic basins depicted by 48,813 landlocked watersheds (yellow) in the 15-second HydroSHEDS drainage basin dataset[40] (accessed from www.hydrosheds.org), supplemented by another 10 small landlocked watersheds (red) depicted in the Global Drainage Basin Database (GDBD)[41] (accessed from www.cger.nies.go.jp/db/gdbd/gdbd_index_e.html). (**b**) 173 endorheic units superimposed by equal-area 3×3 degree spherical cap mascons on the continental surface. Each endorheic unit (shown as one unique color) is one landlocked watershed if its size exceeds a mascon (~100 thousand km^2), or an agglomeration of contiguous or nearby landlocked watersheds until their total area exceeds a mascon. Sporadic landlocked watersheds (filled black polygons) smaller than a mascon and substantially detached from any major endorheic landmass are excluded.

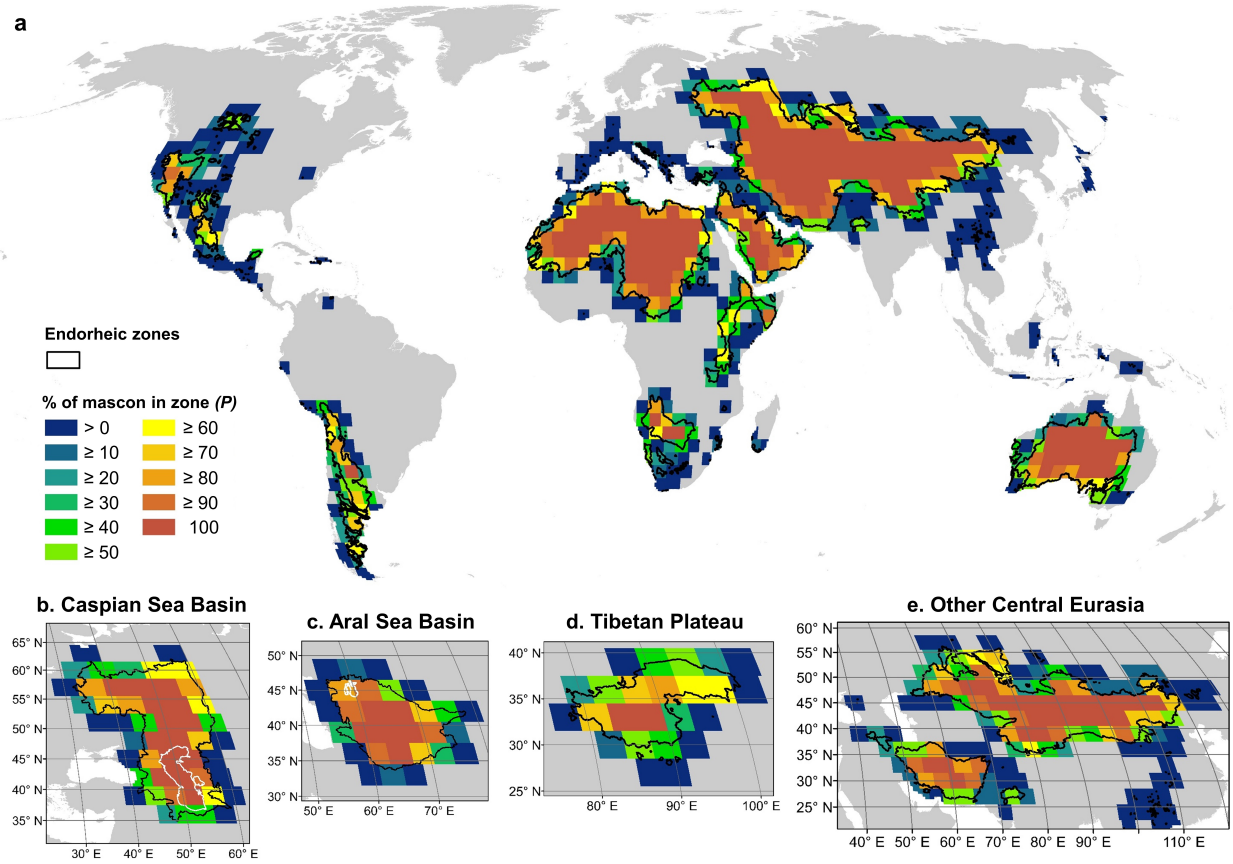

Figure S15. Area proportions (*P*) of spherical cap mascons within the boundary of each endorheic zones. Fringe mascons in each of the six primary continental zones (**a**) and four secondary zones in Central Eurasia (**b**–**e**) are indicated by P values between 0 and 100. For any mascon shared by different zones, its P may vary for each of the shared zones.

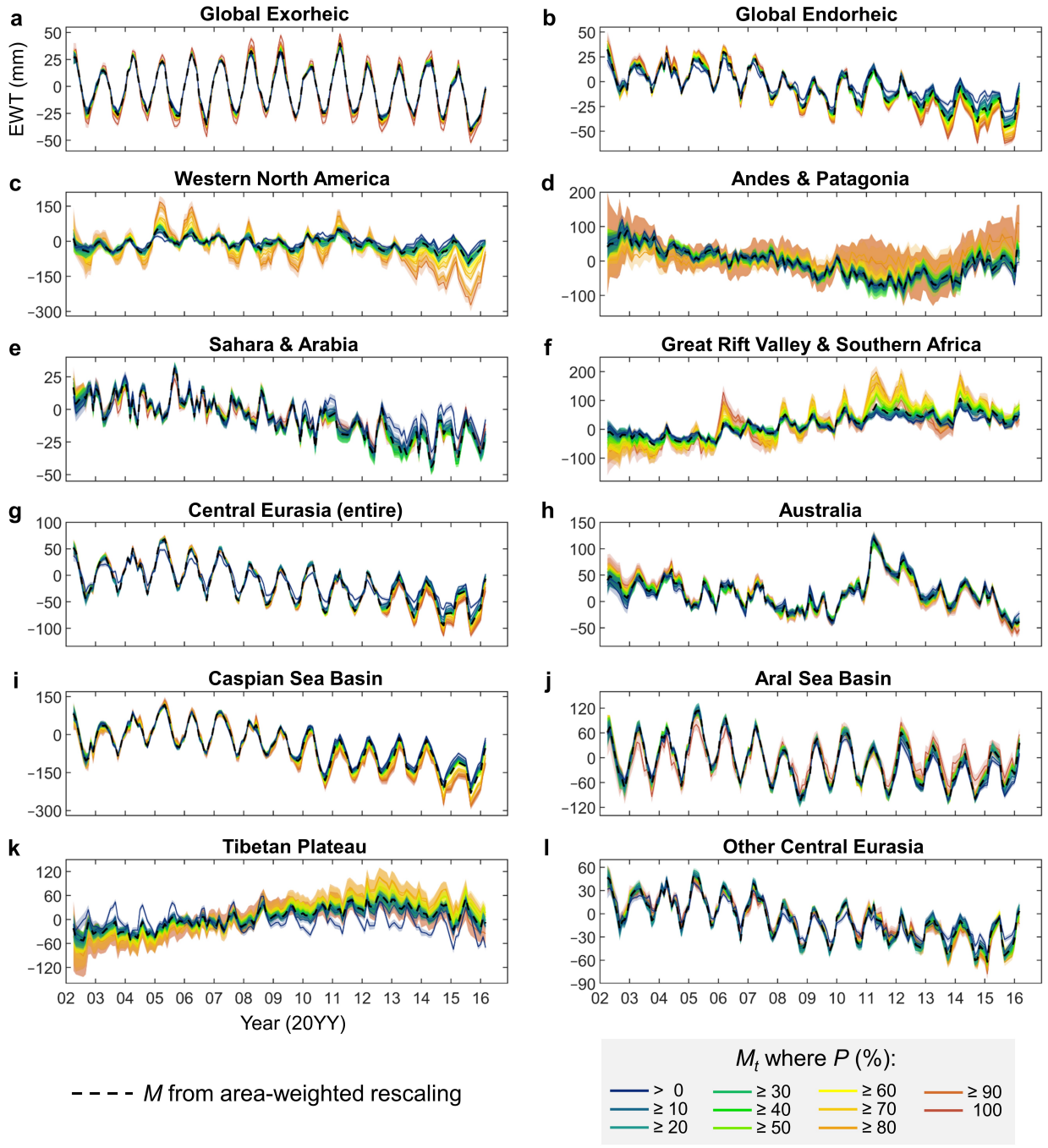

Figure S16. Monthly equivalent water thickness (EWT) from the interior (P = 1.0) to periphery (P > 0) of each global and zonal region during April 2002 to March 2016. (**a**–**b**) Global exorheic and endorheic regions, respectively. (**c**–**h**) Primary endorheic zones. (**i**–**l**) Secondary endorheic zones in Central Eurasia. Dashed black lines represent M calculated using the area-weighted rescaling scheme (refer to Methods in the main paper). Solid color lines represent M_t and their 95% uncertainties ($1.96e_m$) associated with inherent mascon data uncertainties (shown in transparent color shades). Refer to Fig. S17 for their trends.

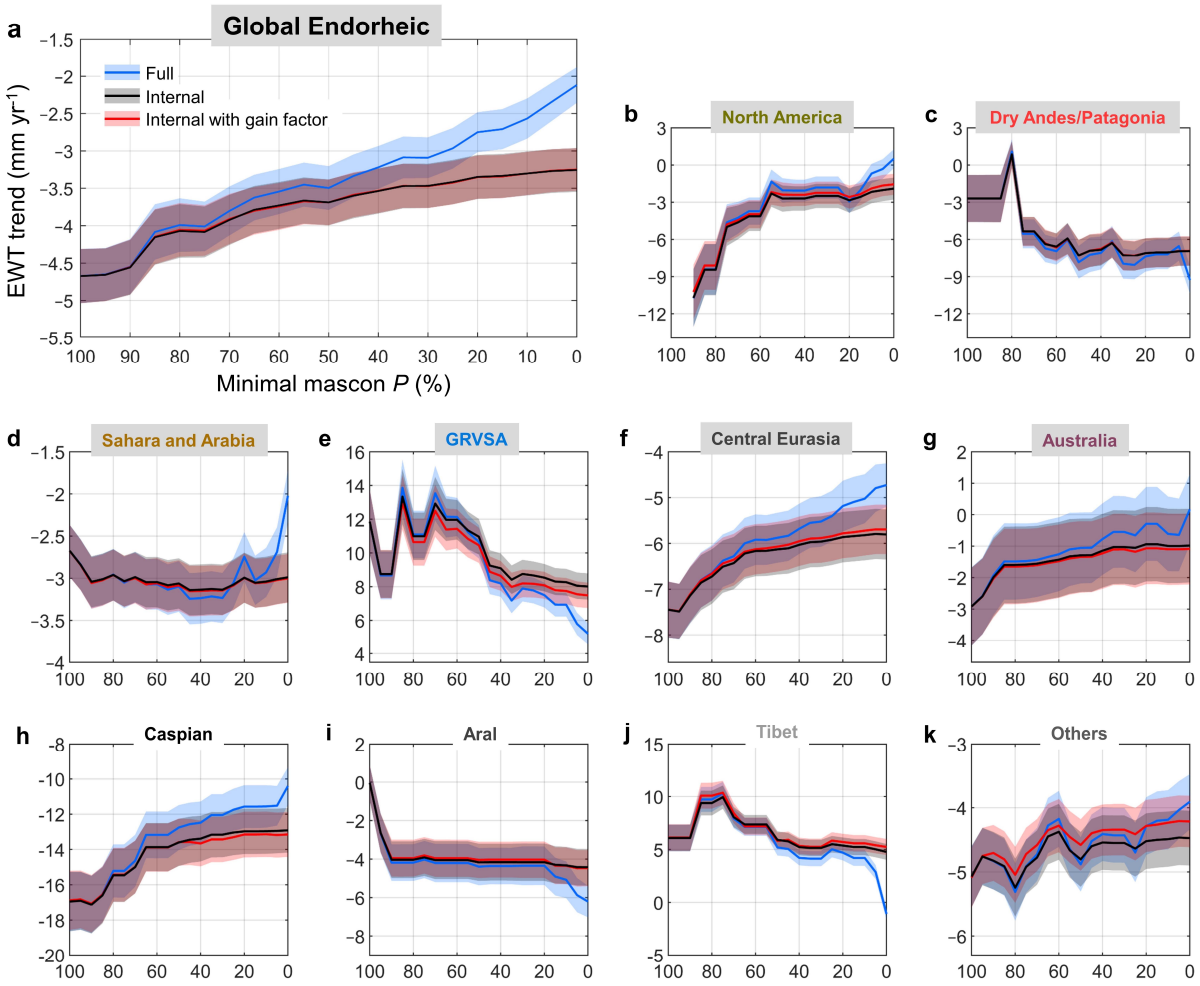

Figure S17. Trends in equivalent water thickness (EWT) from the interior (P = 1.0) to periphery (P > 0) of each global and zonal endorheic region during April 2002 to March 2016. (**a**) Global endorheic system. (**b**–**g**) Primary continental zones. (**h**–**k**) Secondary zones in Central Eurasia. Blue profiles represent the EWT trend in each monthly time series M_t (Fig. S16; calculated using full mascons where P exceeds each minimal threshold t). Red and black profiles represent EWT trends calculated using the internal portions of the mascons where $P \geq t$, with and without the inclusion of the provided 0.5-degree gain factors, respectively. Values when $t = 0$ in the black profiles are used as the final EWT trends reported in the main paper. Transparent shades illustrate the 95% confident interval of each estimated trend associated with inherent mascon data uncertainties.

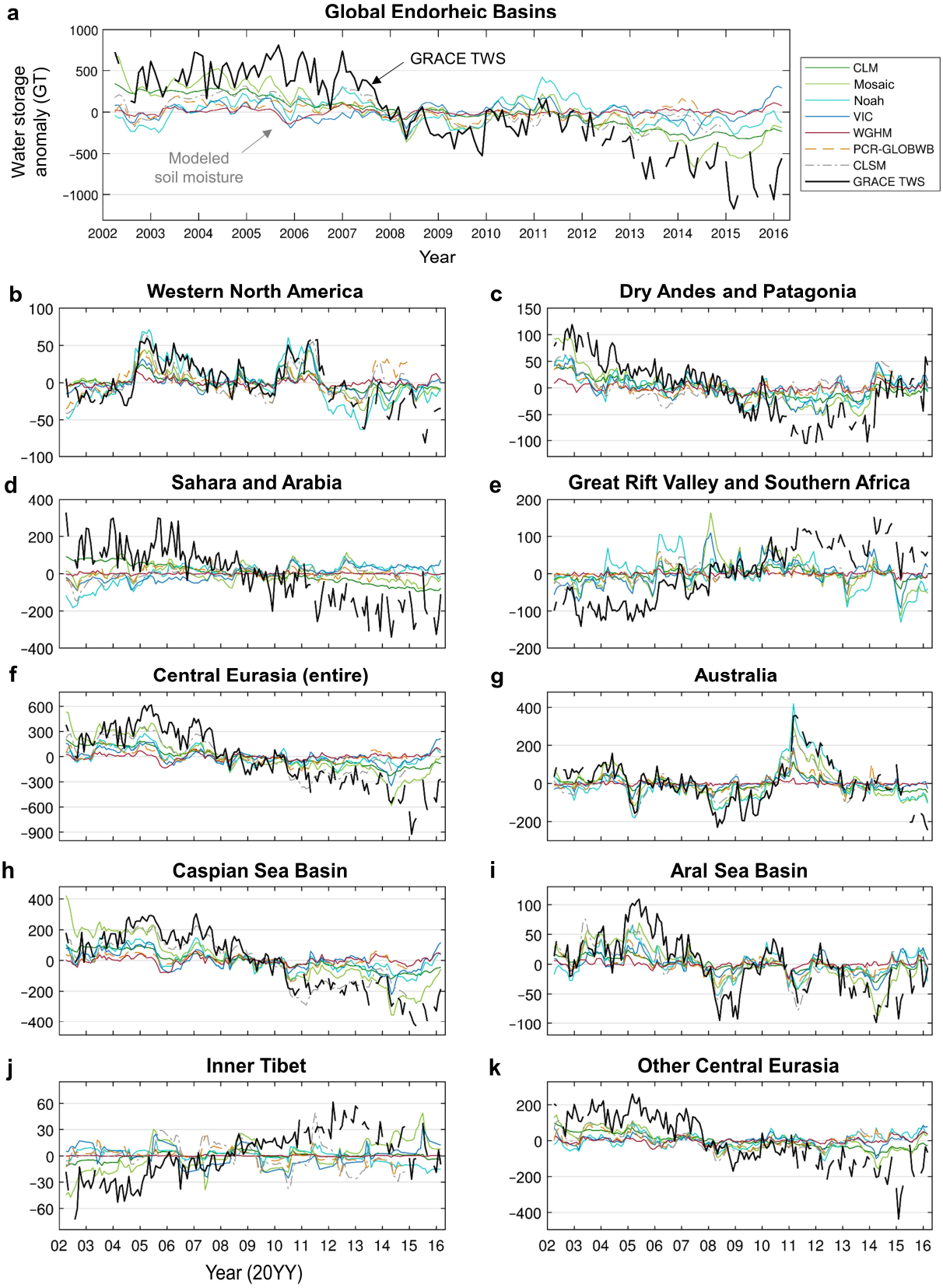
a
Global Endorheic Basins
Water storage anomaly (GT)
GRACE TWS
Modeled soil moisture
CLM
Mosaic
Noah
VIC
WGHM
PCR-GLOBWB
CLSM
GRACE TWS
Year
b
Western North America
c
Dry Andes and Patagonia
d
Sahara and Arabia
e
Great Rift Valley and Southern Africa
f
Central Eurasia (entire)
g
Australia
h
Caspian Sea Basin
i
Aral Sea Basin
j
Inner Tibet
k
Other Central Eurasia
Year (20YY)

Figure S18. Monthly time series of GRACE-observed TWS and model-simulated soil moisture in global and zonal endorheic regions during April 2002 to March 2016. (**a**) Global endorheic regions, respectively. (**b**–**g**) Primary endorheic zones. (**h**–**k**) Secondary endorheic zones in Central Eurasia. All time series are deseasonalized monthly anomalies (i.e., with removal of climatology).

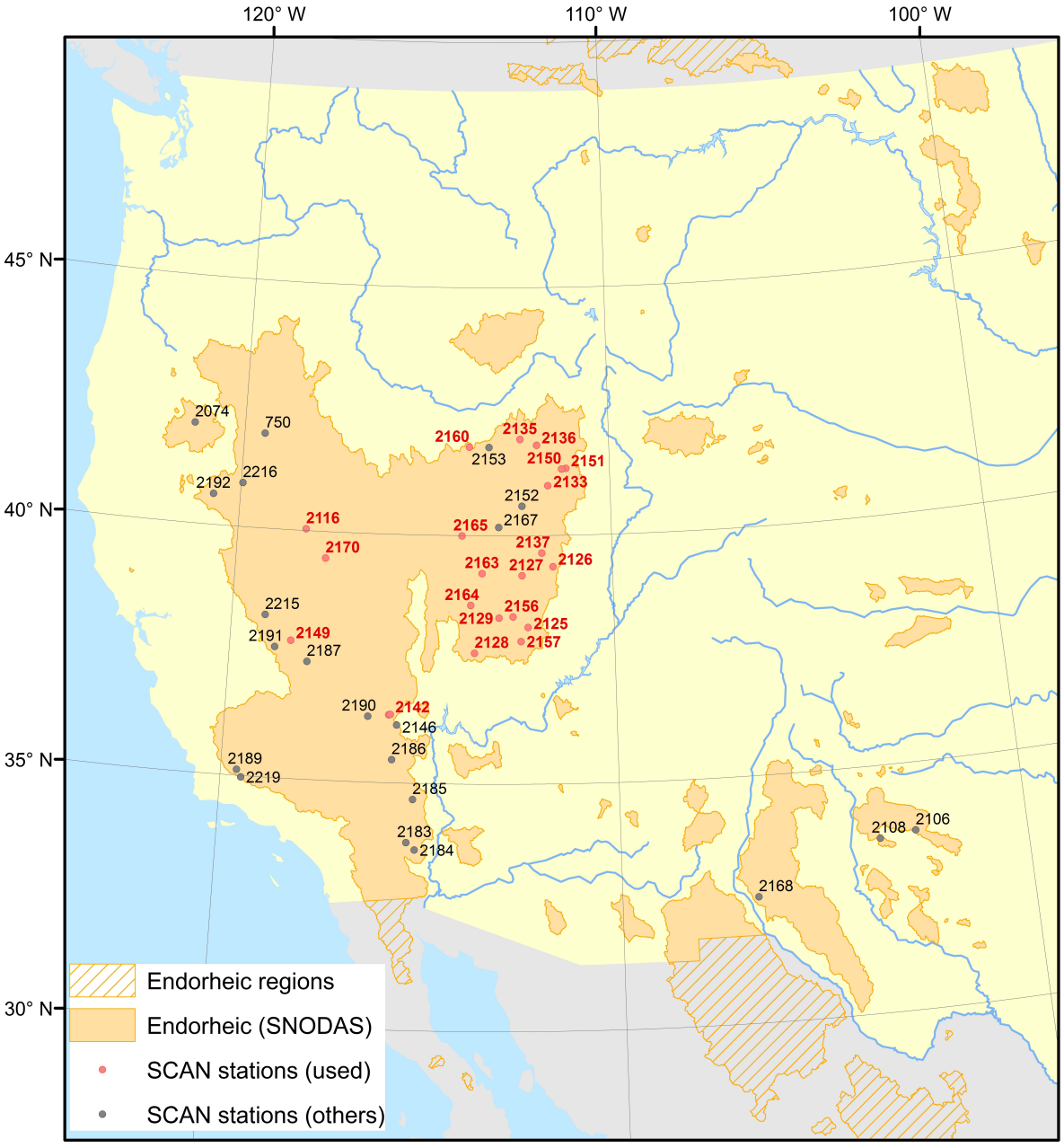

Figure S19. Validation regions for modeled snow water equivalent (SWE) and soil moisture in endorheic North America. Modeled SWE values are validated against the Snow Data Assimilation System (SNODAS) product covering the complete endorheic regions in the conterminous US and a small endorheic portion in Canada (in orange). Modeled soil moisture values are validated against in situ measurements from the US Soil Climate Analysis Network (SCAN). IDs of the 22 used SCAN stations with records exceeding 5 consecutive years are labeled in red (others in black), and their geographic coordinates are provided in Table S6.

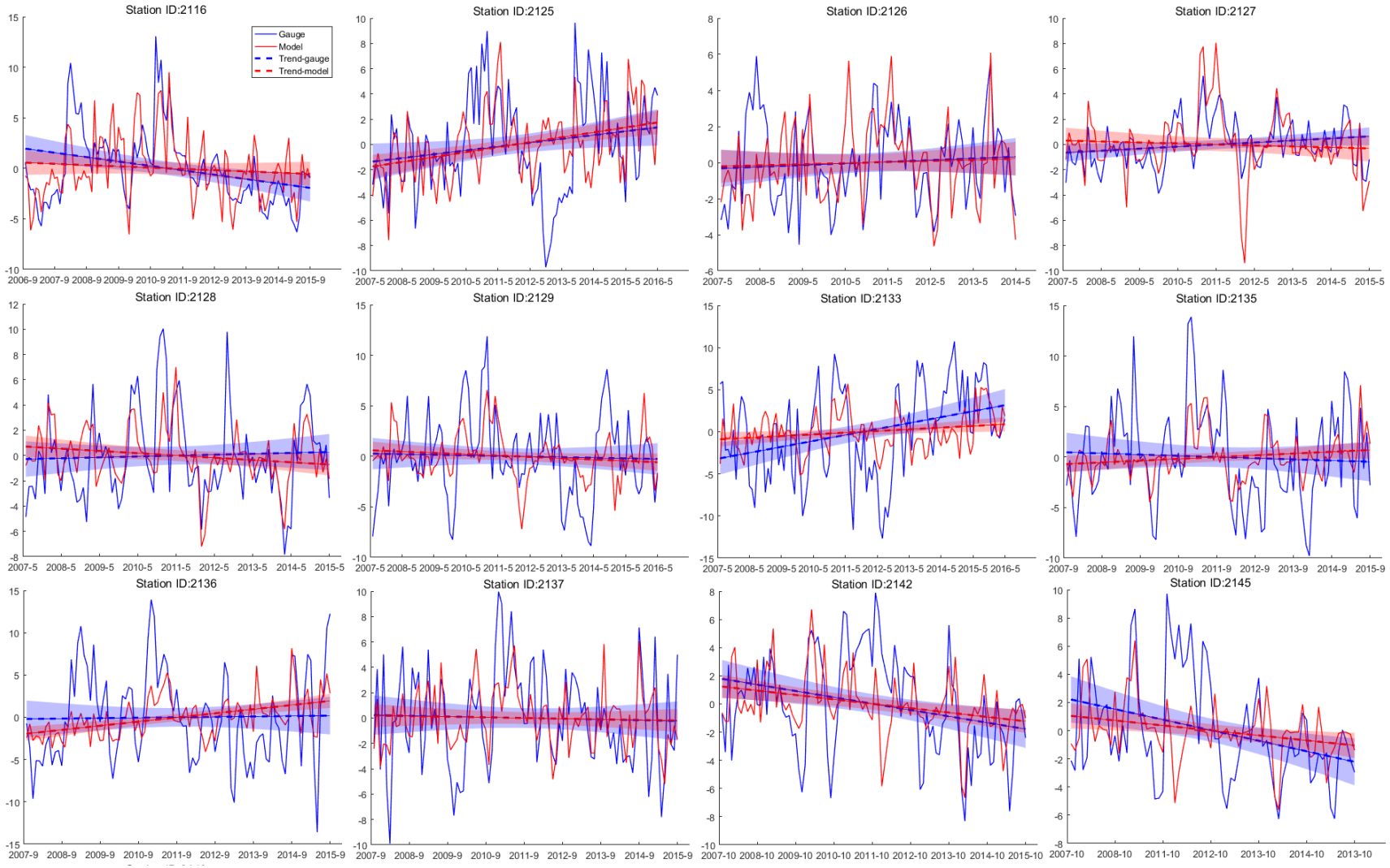

Figure S20 (continued in the next page)

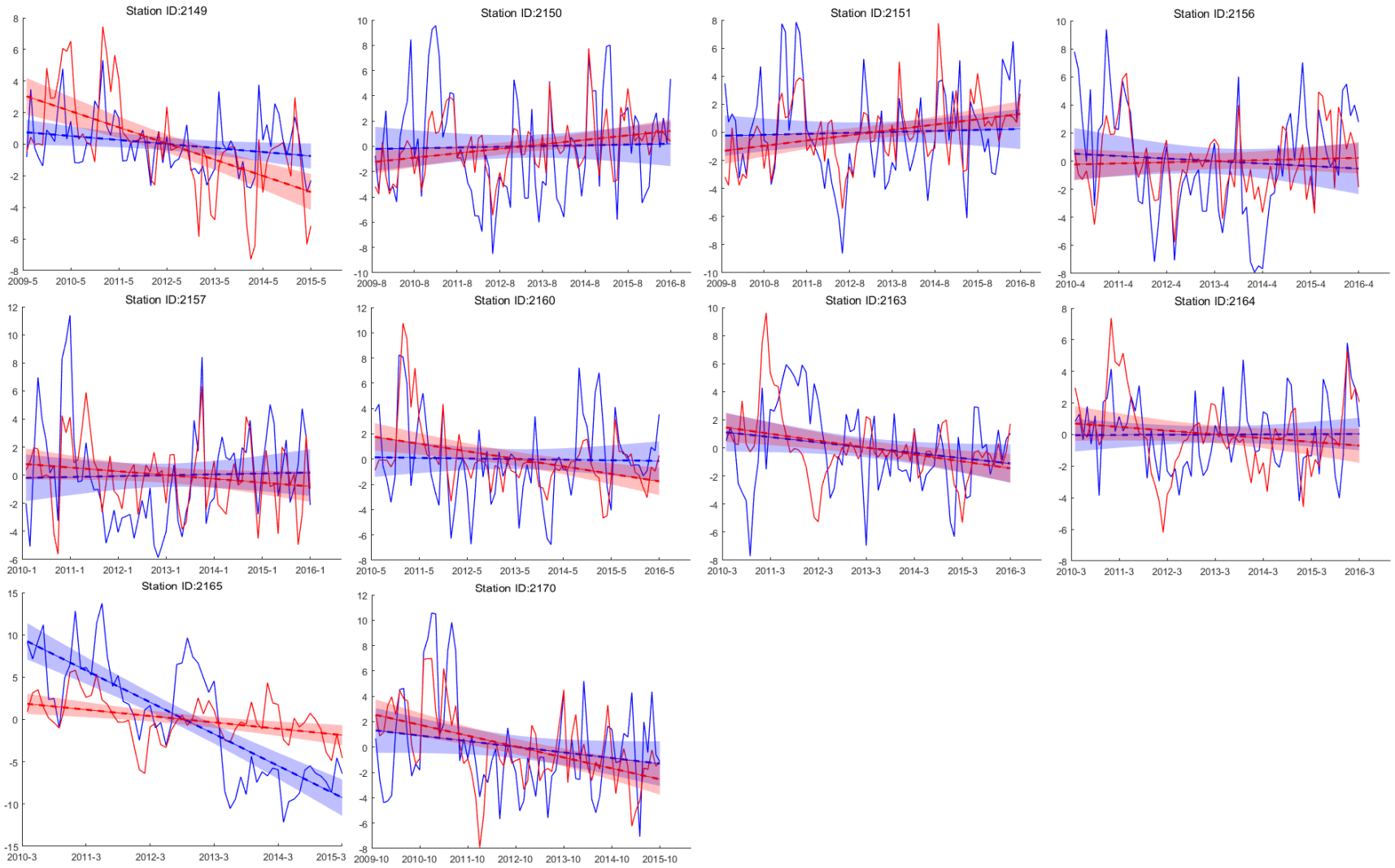

Figure S20. Comparison of monthly time series of soil moisture anomalies from GLDAS model ensemble (VIC, Noah and CLM) and SCAN in situ measurements in endorheic North America. X-axis and Y-axis refer to time (year-month) and deseasonalized soil moisture content (%), respectively. Transparent shades illustrate 95% CIs of the trend fittings. The comparison is

performed for 22 SCAN stations where in situ records exceed 5 consecutive years. Detailed information of these SCAN stations is provided in Fig. S19 and Table S6.

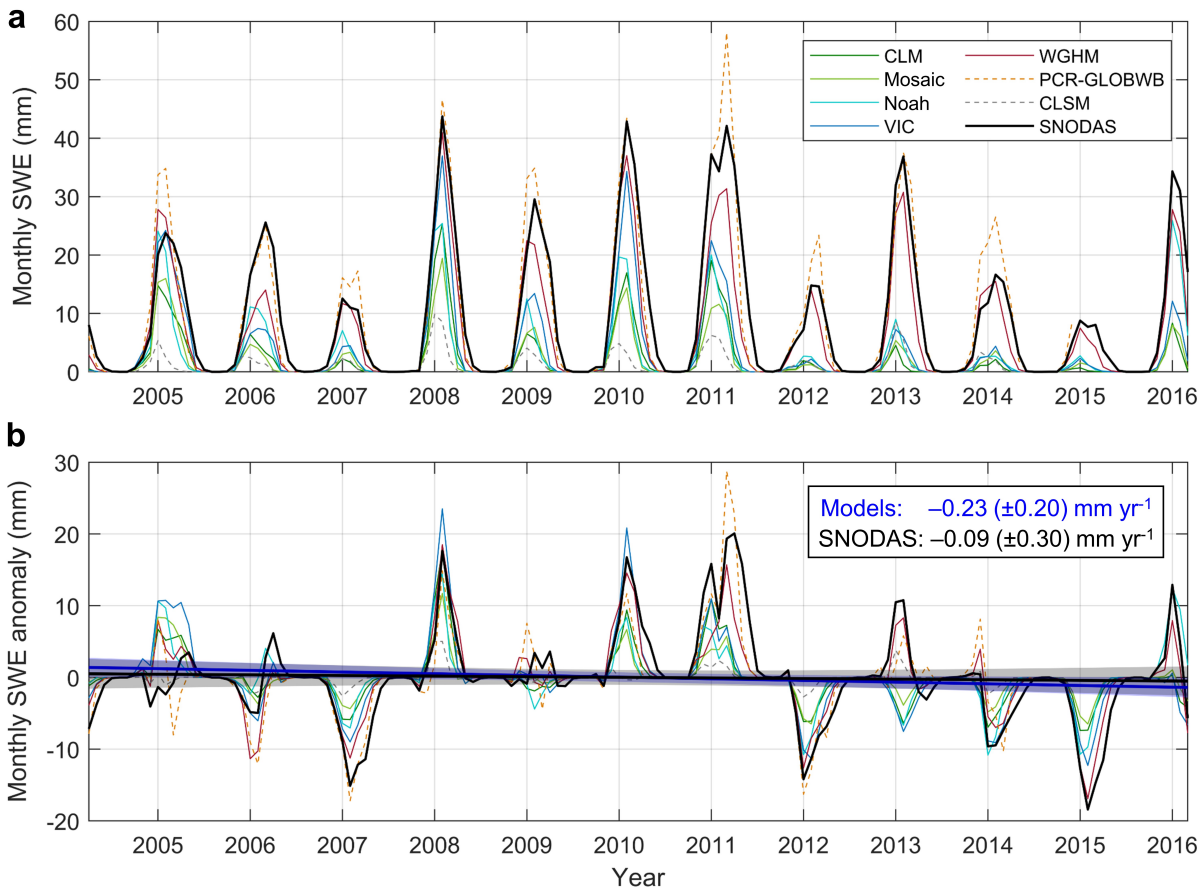

Figure S21. Comparison of snow water equivalent (SWE) between model estimates and the Snow Data Assimilation System (SNOWDAS) product for endorheic North America. Also see Fig. S19 for the endorheic regions covered by the SNODAS product. (**a**) Region-average monthly SWE time series from SNODAS (black line), five LSMs (CLM, Mosaic, Noah, VIC, and CLSM), and two GHMs (WGHM and PCR-GLOBWB). (**b**) Deseasonalized SWE anomalies and their inter-annual trends. Trends for model ensemble and SNODAS are shown in blue and black lines, respectively, and their 95% CIs are illustrated by transparent shades.

Supplementary Tables

Table S1. Applied hydrological models and usage of their water compartments.

Model	Version	Climate forcing	Soil layers		Used compartments		
		Precipitation	Number	Max. depth	Canopy	Snow	Soil moisture
Land surface models (LSM)							
CLM	2.0	CMAP	10	3.433 m	M/U	M/U	M/U
CLSM	3.3	PGMFD	1	Variable	U	U	U
Mosaic		CMAP	3	3.50 m	M/U	M/U	M/U
Noah	3.3	GPCP	4	2.0 m	M/U	M/U	M/U
VIC		CMAP	3	1.9 m	M/U	M/U	M/U
Global hydrological models (GHM)							
WGHM	2.2c	WFDEI	1	Variable	M/U	M/U	U
PCR-GLOBWB	2.0	WFDEI	2	1.5 m	U	U	U

Note: "M/U" indicates that the model product is used for calculating both ensemble means and uncertainties, while "U" indicates that the model output is only used for inferring ensemble uncertainties. "CMAP" is the acronym of the NOAA Climate Prediction Center Merged Analysis of Precipitation[42], "PGMFD" the Global Meteorological Forcing Data set from Princeton University[43], "GPCP" the Global Precipitation Climatology Project)[44], and "WFDEI" the WATCH-Forcing-DATA-ERA-Interim meteorological forcing dataset[45]. Model full names, versions, and accesses are provided here (more relevant details available in Scanlon et al[3]):

- Common Land Model (CLM) 2.0, monthly 1.0º V001, accessed from https://disc.gsfc.nasa.gov/datasets/GLDAS_CLM10_M_V001/summary?keywords=Hydrology.
- Catchment Land Surface Model (CLSM) 3.3, daily 0.25º V2.0, accessed from http://disc.gsfc.nasa.gov/datasets/GLDAS_CLSM025_D_V2.0/summary?keywords=GLDAS%20Catchment. The maximal soil depth varies grid by grid.
- Mosaic model, monthly 1.0º V001, accessed from https://disc.gsfc.nasa.gov/datasets/GLDAS_MOS10_M_V001/summary?keywords=GLDAS%20MOSAIC.
- Noah 3.3, monthly 0.25º V2.1, accessed from https://disc.gsfc.nasa.gov/datasets/GLDAS_NOAH025_M_V2.1/summary?keywords=GLDAS%20NOAH.
- Variable Infiltration Capacity (VIC) model, monthly 1.0º V001, accessed from https://disc.gsfc.nasa.gov/datasets/GLDAS_VIC10_M_V001/summary?keywords=GLDAS%20VIC.
- WaterGAP Global Hydrological Model (WGHM) 2.2c, monthly 0.5º, provided by Hannes Müller Schmied (hannes.mueller.schmied@em.uni-frankfurt.de). The maximal soil depth varies between 0.1 m and 1.4 m depending on land use type.
- PCRaster Global Water Balance (PCR-GLOBWB) model 2.0, monthly 0.5º, provided by Yoshihide Wada (wada@iiasa.ac.at).

Table S2. Glacier mass changes in endorheic Central Eurasia. Estimations are derived from gridded glacier surface elevation changes during 2000–2016 in Brun et al.[46]. Uncertainties represent 95% CIs (two standard deviations).

Secondary zone	Glacierized area		Mass change rate
	km^2	% of zonal area	Gt yr^{-1}
Inner Tibetan Plateau	9,493	0.90	–0.919 (±0.603)
Aral Sea Basin	12,195	0.74	–1.566 (±0.540)
Other Central Eurasia	28,331	0.42	–1.672 (±1.214)
Total	50,019	0.53	–4.157 (±1.459)

Table S3. Glacier mass changes in other endorheic zones. Estimations are referred to Gardner et al.[47] and Falaschi et al.[48]. Uncertainties represent 95% CIs (two standard deviations).

Endorheic zone	Glacierized area		Period	Mass change rate
	km^2	% of zonal area		Gt yr^{-1}
Andes / Patagonia[48]	438	0.03	2000–2012	–0.193 (±0.256)
North America	17	< 0.01	—	—
Caspian Sea Basin[47]	726	0.02	2003–2009	about –0.556

Table S4. Maximum (lag-)correlations between climate indices and TWS anomalies for global exorheic/endorheic basins and each endorheic zone. Numbers that are not parenthesized are Pearson correlation coefficients (r) between each climate index and deseasonalized TWS anomalies, while parenthesized numbers are correlations between each index and changes between deseasonalized TWS anomalies. Strong correlations ($|r| \geq 0.60$) are highlighted as dark bold, moderate correlations ($0.4 < |r| < 0.6$) as dark, and weak/insignificant correlations ($|r| \leq 0.40$) as grey (significance threshold: $|r| > \sim 0.15$ given $\alpha = 0.05$ and $n = 162$). Timescales of the climate indices (first row) are interpreted based on the GRACE era, and may vary in other periods.

Climate var. / Region	*Interannual* ◄——►		*Decadal* ◄——►		*Multidecadal*
	ENSO	**NAO**	**PDO**	**IOD**	**AMO**
Global exorheic	**–0.73** (–0.45)	–0.52 (–0.45)	–0.54 (–0.25)	–0.22 (–0.30)	0.46 (0.54)
Global endorheic	0.27 (0.38)	–0.17 (–0.14)	0.28 (0.31)	–0.33 (–0.19)	0.48 (0.37)
Central Eurasia	0.30 (0.54)	–0.18 (0.19)	0.29 (0.30)	–0.32 (0.18)	0.45 (–0.23)
Caspian Sea	0.20 (0.35)	–0.15 (0.26)	0.22 (0.34)	–0.28 (0.18)	0.34 (0.13)
Aral Sea	0.44 (0.48)	–0.23 (0.27)	0.37 (0.27)	–0.41 (–0.20)	**0.70** (–0.50)
Tibet	–0.57 (–0.25)	–0.32 (–0.33)	**–0.65** (–0.29)	0.46 (–0.03)	–0.23 (0.13)
Others	0.44 (**0.60**)	–0.10 (0.20)	0.40 (0.37)	–0.37 (0.19)	0.49 (–0.33)
Sahara/Arabia	0.35 (0.34)	–0.19 (0.28)	0.37 (0.30)	–0.33 (–0.28)	0.37 (–0.28)
Andes/Patagonia	**0.60** (0.40)	0.55 (0.54)	**0.69** (0.27)	–0.48 (–0.11)	0.22 (–0.35)
Australia	–0.46 (–0.32)	–0.52 (–0.59)	–0.30 (–0.12)	–0.11 (–0.19)	0.42 (0.41)
North America	–0.59 (0.35)	–0.47 (–0.22)	–0.46 (0.19)	–0.26 (–0.36)	**0.61** (0.37)
GRVSA	–0.47 (–0.29)	–0.25 (–0.33)	–0.45 (–0.21)	0.39 (–0.22)	–0.34 (0.30)

Note: Times series of climate indices are accessed from the NOAA's Earth System Research Laboratory (https://www.esrl.noaa.gov/psd/data/climateindices/list):

- Multivariate ENSO Index (MEI): www.esrl.noaa.gov/psd/enso/mei/table.html (accessed approximately 10/1/2017)
- NAO index: www.cpc.ncep.noaa.gov/products/precip/CWlink/pna/norm.nao.monthly.b5001.current.ascii.table (accessed 7/31/2018)
- PDO index: http://research.jisao.washington.edu/pdo/PDO.latest (accessed 7/31/2018)
- Dipole Mode Index (DMI) for IOD: www.esrl.noaa.gov/psd/gcos_wgsp/Timeseries/Data/dmi.long.data (accessed 8/8/2018)
- AMO index: www.esrl.noaa.gov/psd/data/correlation/amon.us.data (accessed 7/31/2018)

Table S5. Surface water storage changes and contributions of different storage components in global and zonal endorheic basins. Uncertainties represent 95% CIs (two standard deviations).

Endorheic Region	Area	Surface Water (SW)	Lakes and Reservoirs		Glaciers		Snow Water		Canopic Water	
	10^6 km^2	Gt yr^{-1}	Gt yr^{-1}	% of ΔSW	Gt yr^{-1}	% of ΔSW	Gt yr^{-1}	% of ΔSW	Gt yr^{-1}	% of ΔSW
Central Eurasia	12.69	–35.40 (±6.19)	–27.92 (±5.72)	78.85 (±16.16)	–4.16 (±1.45)	11.74 (±4.10)	–3.32 (±1.86)	9.39 (±5.24)	–0.005 (±0.005)	0.015 (±0.014)
Caspian Sea	3.17	–28.22 (±2.62)	–27.83 (±2.43)	98.62 (±8.61)	——	——	–0.38 (±0.97)	1.36 (±3.43)	–0.004 (±0.003)	0.013 (±0.011)
Aral Sea	1.65	–6.04 (±0.86)	–3.64 (±0.56)	60.26 (±9.31)	–1.57 (±0.54)	25.91 (±8.89)	–0.84 (±0.37)	13.83 (±6.09)	0.000 (±0.001)	0.004 (±0.014)
Tibet	1.06	4.13 (±1.27)	5.16 (±0.96)	124.90 (±23.32)	–0.92 (±0.60)	–22.23 (±14.51)	–0.11 (±0.56)	–2.66 (±13.56)	0.000 (±0.001)	–0.009 (±0.013)
Others	6.80	–5.27 (±3.11)	–1.60 (±2.71)	30.43 (±51.50)	–1.67 (±1.21)	31.73 (±22.91)	–1.99 (±0.91)	37.83 (±17.36)	–0.001 (±0.002)	0.017 (±0.045)
Sahara / Arabia	11.07	0.01 (±0.53)	0.05 (±0.53)	579.62 (±5958.55)	——	——	–0.04 (±0.02)	–472.73 (±231.65)	–0.001 (±0.001)	–6.888 (±9.600)
Andes / Patagonia	1.38	–2.88 (±1.40)	–2.72 (±1.40)	94.37 (±48.73)	——	——	–0.16 (±0.09)	5.60 (±3.14)	–0.001 (±0.001)	0.033 (±0.022)
Australia	4.13	–0.03 (±1.73)	–0.03 (±1.73)	96.97 (±5417.08)	——	——	0.00 (±0.00)	0.30 (±0.39)	–0.001 (±0.002)	2.728 (±4.773)
North America	1.33	–0.43 (±0.58)	–0.33 (±0.57)	76.71 (±132.83)	——	——	–0.10 (±0.14)	23.03 (±32.25)	–0.001 (±0.001)	0.256 (±0.183)
GRVSA	2.07	0.37 (±0.60)	0.37 (±0.60)	100.38 (±162.90)	——	——	0.00 (±0.00)	–0.02 (±0.02)	–0.001 (±0.001)	–0.354 (±0.301)
Global	**32.67**	**–38.36 (±10.52)**	**–30.57 (±10.24)**	**79.69 (±26.70)**	**–4.16 (±1.45)**	**10.84 (±3.78)**	**–3.63 (±1.90)**	**9.45 (±4.96)**	**–0.010 (±0.006)**	**0.026 (±0.015)**

Table S6. Validation of monthly soil moisture time series from GLDAS model ensemble using SCAN in situ soil moisture measurements in endorheic North America. Validation includes Pearson correlation coefficient (*r*) and interannual trend (% yr^{-1}) between deseasonlized monthly time series of modeled and in situ soil moisture contents (%), for a total of 22 SCAN stations (see Fig. S19 for locations) where measurement records exceed 5 consecutive years. Trend uncertainties represent 95% CIs (two standard deviations). The GLDAS model ensemble for total soil layers includes VIC, Noah, CLM and Mosaic, and the 0-10 cm ensemble only includes VIC, Noah, and CLM as the Mosaic model does not contain the 0-10 cm soil layer.

SCAN soil moisture station				Total soil layers	Soil layers (0-10 cm)		
ID	Name	Longitude	Latitude	*r*	*r*	Trend (in situ)	Trend (modeled)
2116	Lovelock NNR	40.0333	–118.1776	0.470**	0.629**	–0.436 (±0.134)	–0.125 (±0.120)
2125	Circleville	38.1513	–112.2512	0.372**	0.348**	0.304 (±0.142)	0.391 (±0.092)
2126	Ephraim	39.368	–111.5780	0.054	0.466**	0.092 (±0.132)	0.061 (±0.118)
2127	Holden	39.1922	–112.4016	0.556**	0.690**	0.162 (±0.079)	–0.078 (±0.114)
2128	Enterprise	37.6334	–113.6432	0.630**	0.571**	0.070 (±0.157)	–0.180 (±0.096)
2129	Milford	38.342	–113.0105	0.394**	0.460**	–0.059 (±0.155)	–0.132 (±0.084)
2133	Morgan	40.9999	–111.6856	0.167	0.405**	0.707 (±0.190)	0.200 (±0.085)
2135	Blue Creek	41.9353	–112.4336	0.578**	0.491**	–0.118 (±0.215)	0.176 (±0.095)
2136	Cache Junction	41.8157	–111.9804	0.422**	0.535**	0.049 (±0.246)	0.490 (±0.094)
2137	Nephi	39.6455	–111.8704	0.597**	0.615**	–0.058 (±0.173)	–0.048 (±0.101)
2142	Trough Springs	36.3736	–115.7813	0.599**	0.440**	–0.450 (±0.149)	–0.312 (±0.092)
2145	Charkiln	36.3665	–115.8205	——	0.283*	–0.748 (±0.247)	–0.354 (±0.133)
2149	Marble Creek	37.7777	–118.4209	0.572**	0.657**	–0.253 (±0.118)	–1.024 (±0.170)
2150	Chicken Ridge	41.3314	–111.3036	0.471**	0.588**	0.059 (±0.223)	0.354 (±0.116)
2151	Buffalo Jump	41.3436	–111.1880	——	0.632**	0.070 (±0.184)	0.378 (±0.118)
2156	Manderfield	38.3665	–112.6429	0.714**	0.586**	–0.179 (±0.272)	0.079 (±0.168)
2157	Panguitch	37.8698	–112.4344	0.540**	0.462**	0.064 (±0.248)	–0.269 (±0.163)
2160	Grouse Creek	41.7785	–113.8205	0.665**	0.546**	–0.048 (±0.229)	–0.594 (±0.161)
2163	Tule Valley	39.2372	–113.4587	0.370**	0.098	–0.377 (±0.204)	–0.491 (±0.152)
2164	Hals Canyon	38.5945	–113.7510	0.298*	0.454**	0.012 (±0.154)	–0.236 (±0.162)
2165	Goshute	39.99	–114.0003	——	0.557**	–3.758 (±0.386)	–0.751 (±0.215)
2170	Porter Canyon	39.4654	–117.6207	0.753**	0.553**	–0.443 (±0.262)	–0.858 (±0.181)

Note: SCAN in situ soil moisture data sets can be accessed at www.wcc.nrcs.usda.gov/scan. The symbols ** and * represent *p*-values that are less than 0.01 and 0.05, respectively.

Supplementary references

1 National Operational Hydrologic Remote Sensing Center. Snow Data Assimilation System (SNODAS) Data Products at NSIDC, Version 1. *National Snow and Ice Data Center (NSIDC), Boulder, Colorado USA*, doi:10.7265/N5TB14TC (2004).

2 Siebert, S. *et al*. Development and validation of the global map of irrigation areas. *Hydrol. Earth Syst. Sc.* **9**, 535-547 (2005).

3 Scanlon, B. R. *et al.* Global models underestimate large decadal declining and rising water storage trends relative to GRACE satellite data. *P. Natl. Acad. Sci. USA*, doi:10.1073/pnas.1704665115 (2018).

4 Wada, Y., Wisser, D. & Bierkens, M. F. P. Global modeling of withdrawal, allocation and consumptive use of surface water and groundwater resources. *Earth Syst. Dynam.* **5**, 15-40 (2014).

5 Taylor, R. G. et al. Ground water and climate change. *Nat. Clim. Change* **3**, 322-329 (2013).

6 DeAngelis, A. et al. Evidence of enhanced precipitation due to irrigation over the Great Plains of the United States. *J. Geophys. Res. Atmos.* **115**, D15115 (2010).

7 Douglas, E. M., Beltran-Przekurat, A., Niyogi, D., Pielke, R. A. & Vörösmarty, C. J. The impact of agricultural intensification and irrigation on land-atmosphere interactions and Indian monsoon precipitation - A mesoscale modeling perspective. *Global Planet. Change* **67**, 117-128 (2009).

8 Hurrell, J. W. Influence of variations in extratropical wintertime teleconnections on Northern Hemisphere temperature. *Geophys. Res. Lett.* **23**, 665-668 (1996).

9 Alexander, M. A. et al. The atmospheric bridge: The influence of ENSO teleconnections on air-sea interaction over the global oceans. *J. Climate* **15**, 2205-2231 (2002).

10 Taylor, R. G. et al. Evidence of the dependence of groundwater resources on extreme rainfall in East Africa. *Nat. Clim. Change* **3**, 374-378 (2013).

11 Phillips, T., Nerem, R. S., Fox-Kemper, B., Famiglietti, J. S. & Rajagopalan, B. The influence of ENSO on global terrestrial water storage using GRACE. *Geophys. Res. Lett.* **39**, L16705 (2012).

12 Zhang, Z. Z., Chao, B. F., Chen, J. L. & Wilson, C. R. Terrestrial water storage anomalies of Yangtze River Basin droughts observed by GRACE and connections with ENSO. *Global Planet. Change* **126**, 35-45 (2015).

13 Ni, S. N. et al. Global Terrestrial Water Storage Changes and Connections to ENSO Events. *Surv. Geophys.* **39**, 1-22 (2018).

14 Cazenave, A. et al. The rate of sea-level rise. *Nat. Clim. Change* **4**, 358-361 (2014).

15 Reager, J. T. et al. A decade of sea level rise slowed by climate-driven hydrology. *Science* **351**, 699-703 (2016).

16 Wada, Y. et al. Recent Changes in Land Water Storage and its Contribution to Sea Level Variations. *Surv. Geophys.* **38**, 131-152.

17 Mantua, N. J., Hare, S. R., Zhang, Y., Wallace, J. M. & Francis, R. C. A Pacific interdecadal climate oscillation with impacts on salmon production. *B. Am. Meteorol. Soc.* **78**, 1069-1079 (1997).

18 Saji, N. H., Goswami, B. N., Vinayachandran, P. N. & Yamagata, T. A dipole mode in the tropical Indian Ocean. *Nature* **401**, 360-363 (1999).

19 Lim, E. P. & Hendon, H. H. Causes and Predictability of the Negative Indian Ocean Dipole and Its Impact on La Nina During 2016. *Sci. Rep.* **7**, 12619 (2017).

20 Kerr, R. A. A North Atlantic climate pacemaker for the centuries. *Science* **288**, 1984-1986 (2000).

21 de Linage, C., Kim, H., Famiglietti, J. S. & Yu, J. Y. Impact of Pacific and Atlantic sea surface temperatures on interannual and decadal variations of GRACE land water storage in tropical South America. *J. Geophy. Res.-Atmos.* **118**, 10811-10829 (2013).

22 Nicholson, S. E. & Kim, E. The relationship of the El Nino Southern oscillation to African rainfall. *Int. J. Climatol.* **17**, 117-135 (1997).
23 Kumar, K. K., Rajagopalan, B. & Cane, M. A. On the weakening relationship between the Indian monsoon and ENSO. *Science* **284**, 2156-2159 (1999).
24 Ronchail, J. et al. Interannual rainfall variability in the Amazon basin and sea-surface temperatures in the equatorial Pacific and the tropical Atlantic Oceans. *Int. J. Climatol.* **22**, 1663-1686 (2002).
25 Zhou, T. J., Yu, R. C., Li, H. M. & Wang, B. Ocean forcing to changes in global monsoon precipitation over the recent half-century. *J. Climate* **21**, 3833-3852 (2008).
26 Molinier, M. et al. Hydrological variability in the Amazon drainage basin and African tropical basins. *Hydrol. Processes* **23**, 3245-3252 (2009).
27 Wise, E. K. Spatiotemporal variability of the precipitation dipole transition zone in the western United States. *Geophys. Res. Lett.* **37**, L07706 (2010).
28 Yang, P., Xia, J., Zhan, C. S., Zhang, Y. Y. & Chen, J. Study on the Variation of Terrestrial Water Storage and the Identification of Its Relationship with Hydrological Cycle Factors in the Tarim River Basin, China. *Adv. Meteorol.*, 5086854 (2017).
29 Frajka-Williams, E., Beaulieu, C. & Duchez, A. Emerging negative Atlantic Multidecadal Oscillation index in spite of warm subtropics. *Sci. Rep.* **7**, 11224 (2017).
30 Daniels, L. D. & Veblen, T. T. ENSO effects on temperature and precipitation of the Patagonian-Andean region: Implications for biogeography. *Phys. Geogr.* **21**, 223-243 (2000).
31 Cai, W. J., van Rensch, P., Cowan, T. & Hendon, H. H. Teleconnection Pathways of ENSO and the IOD and the Mechanisms for Impacts on Australian Rainfall. *J. Climate* **24**, 3910-3923 (2011).
32 van Dijk, A. I. J. M. et al. The Millennium Drought in southeast Australia (2001-2009): Natural and human causes and implications for water resources, ecosystems, economy, and society. *Water Resour. Res.* **49**, 1040-1057 (2013).
33 Rodell, M. et al. Emerging trends in global freshwater availability. *Nature* **557**, 650-659 (2018).
34 Richey, A. S. et al. Quantifying renewable groundwater stress with GRACE. *Water Resour. Res.* **51**, 5217-5238 (2015).
35 Sheng, Y. *et al.* Representative lake water extent mapping at continental scales using multi-temporal Landsat-8 imagery. *Remote Sens. Environ.* **185**, 129-141 (2016).
36 Crétaux, J. F. *et al.* SOLS: A lake database to monitor in the Near Real Time water level and storage variations from remote sensing data. *Adv. Space Res.* **47**, 1497-1507 (2011).
37 Schwatke, C., Dettmering, D., Bosch, W. & Seitz, F. DAHITI - an innovative approach for estimating water level time series over inland waters using multi-mission satellite altimetry. *Hydrol. Earth Syst. Sc.* **19**, 4345-4364 (2015).
38 RGI Consortium. *Randolph Glacier Inventory – A Dataset of Global Glacier Outlines: Version 6.0: Technical Report* (Global Land Ice Measurements from Space, Boulder, Colorado, USA, 2017) doi:10.7265/N5-RGI-60.
39 Rahmstorf, S., Foster, G. & Cahill, N. Global temperature evolution: recent trends and some pitfalls. *Environ.l Res. Lett.* **12**, 054001 (2017).
40 Lehner, B., Verdin, K. & Jarvis, A. New global hydrography derived from spaceborne elevation data. *Eos, Trans. Amer. Geophys. Union* **89**, 93-94 (2008).
41 Masutomi, Y., Inui, Y., Takahashi, K. & Matsuoka, Y. Development of highly accurate global polygonal drainage basin data. *Hydrol. Processes* **23**, 572-584 (2009).
42 Xie, P. P. & Arkin, P. A. Global precipitation: A 17-year monthly analysis based on gauge observations, satellite estimates, and numerical model outputs. *B. Am. Meteorol. Soc.* **78**, 2539-2558 (1997).

43 Sheffield, J., Goteti, G. & Wood, E. F. Development of a 50-year high-resolution global dataset of meteorological forcings for land surface modeling. *J. Climate* **19**, 3088-3111 (2006).
44 Adler, R. F. *et al.* The version-2 global precipitation climatology project (GPCP) monthly precipitation analysis (1979-present). *J. Hydrometeorol.* **4**, 1147-1167 (2003).
45 Weedon, G. P. *et al.* The WFDEI meteorological forcing data set: WATCH Forcing Data methodology applied to ERA-Interim reanalysis data. *Water Resour. Res.* **50**, 7505-7514 (2014).
46 Brun, F., Berthier, E., Wagnon, P., Kääb, A. & Treichler, D. A spatially resolved estimate of High Mountain Asia glacier mass balances from 2000 to 2016. *Nat. Geosci.* **10**, 668-673 (2017).
47 Gardner, A. S. *et al.* A reconciled estimate of glacier contributions to sea level rise: 2003 to 2009. *Science* **340**, 852-857 (2013).
48 Falaschi, D. *et al.* Mass changes of alpine glaciers at the eastern margin of the Northern and Southern Patagonian Icefields between 2000 and 2012. *J. Glaciol.* **63**, 258-272 (2017).